

What determines the formation and characteristics of protoplanetary discs?

Patrick Hennebelle¹, Benoit Commerçon³, Yueh-Ning Lee^{4,2,1}, and Sébastien Charnoz²

¹ AIM, CEA, CNRS, Université Paris-Saclay, Université Paris Diderot, Sorbonne Paris Cité, F-91191 Gif-sur-Yvette, France,

² Institut de Physique du Globe de Paris, Sorbonne Paris Cité, Université Paris Diderot, UMR 7154 CNRS, F-75005 Paris, France

³ Univ Lyon, Ens de Lyon, Univ Lyon1, CNRS, Centre de Recherche Astrophysique de Lyon UMR5574, F-69007, Lyon, France

⁴ Department of Earth Sciences, National Taiwan Normal University, 88, Sec. 4, Ting-Chou Road, Taipei 11677, Taiwan

Received —; accepted —

ABSTRACT

Context. Planets form in protoplanetary discs. Their masses, distribution, and orbits sensitively depend on the structure of the protoplanetary discs. However, what sets the initial structure of the discs in terms of mass, radius and accretion rate is still unknown.

Aims. It is therefore of great importance to understand exactly how protoplanetary discs form and what determine their physical properties. We aim at quantifying the role of the initial dense core magnetisation, rotation, turbulence and misalignment between rotation and magnetic field axis as well as the role of the accretion scheme onto the central object.

Methods. We perform non-ideal MHD numerical simulations using the adaptive mesh refinement code Ramses, of a collapsing, one solar mass, molecular core to study the disc formation and early, up to 100 kyr, evolution, paying great attention to the impact of numerical resolution and accretion scheme.

Results. We found that while the mass of the central object is almost independent of the numerical parameters such as the resolution and the accretion scheme onto the sink particle, the disc mass, and to a lower extent its size, heavily depend on the accretion scheme, which we found, is itself resolution dependent. This implies that the accretion onto the star and through the disc are largely decoupled. For a relatively large domain of initial conditions (except at low magnetisation), we found that the properties of the disc do not change too significantly. In particular both the level of initial rotation and turbulence do not influence the disc properties provide the core is sufficiently magnetized. After a short relaxation phase, the disc settles in a stationary state. It then slowly grows in size but not in mass. The disc itself is weakly magnetized but its immediate surrounding is on the contrary highly magnetized.

Conclusions. Our results show that the disc properties eventually depend on the inner boundary condition, i.e. the accretion scheme onto the central object, suggesting that the disc mass is eventually controlled by the small scale accretion process, possibly the star-disc interaction. Because of ambipolar diffusion and its significant resistivity, the disc diversity remains limited and except for low magnetisation, their properties are weakly sensitive to initial conditions such as rotation and turbulence.

Key words. ISM: clouds – ISM: structure – Turbulence – gravity – Stars: formation

1. Introduction

It is well established that planets form within circumstellar discs, and therefore knowing the conditions under which these protoplanetary discs form as well as their physical characteristics such as mass and size is of fundamental importance (Testi et al. 2014; Dutrey et al. 2014). While most discs observed so far are located around objects that are not any more embedded, i.e. T-Tauri stars, there are increasing evidences that the discs form early during the class-0 stage (Jørgensen et al. 2009; Maury et al. 2010; Murillo et al. 2013; Ohashi et al. 2014; Tobin et al. 2016; Maury et al. 2019). While the statistics remain hampered by large uncertainties, it seems that there is a clear trend for the discs at this early stage to be limited in size with most discs having a radii below 60 AU, and possibly even smaller. Understanding this initial phase is of primordial importance to get the complete history of the process, but also because the mass of the discs observed around T-Tauri stars may not be massive enough to explain the mass of the observed planets (Greaves & Rice 2010; Najita & Kenyon 2014; Manara et al. 2018), suggesting that planet formation may start early after the protostar formation during the infall envelope while the disc is still fed by fresh ISM materials.

From a theoretical point of view, much progress has been made in the last decade regarding the formation of protoplanetary discs during the collapse of prestellar cores. One of the major outcome of the first calculations of magnetized collapse (e.g. Allen et al. 2003; Galli et al. 2006; Price & Bate 2007; Hennebelle & Fromang 2008; Li et al. 2014; Wurster & Li 2018; Hennebelle & Inutsuka 2019), is that magnetic braking could be so efficient that disc formation may be entirely prevented, a process named as catastrophic braking. Further studies have shown that the aligned configuration assumed in these calculations was however a significant oversimplification and that discs should form in magnetized clouds, although the discs are smaller in size and fragment less than in the absence of magnetic field. Three reasons have been proposed to explain how magnetic braking is reduced i) the magnetic field and the rotation axis are misaligned (Joos et al. 2012; Li et al. 2013; Gray et al. 2018), ii) turbulence diffuses the magnetic flux outwards (Santos-Lima et al. 2012; Joos et al. 2013), iii) tangled magnetic field is inefficient to transport momentum (Seifried et al. 2013). Note that Gray et al. (2018) carried out calculations with a turbulent velocity field in which the angular momentum is aligned with the magnetic field. They found that discs do not form or are much smaller than when

there is no particular alignment. This led them to conclude that misalignment is the main effect.

The second over-simplification which has been made in the first series of studies, is the assumption of ideal MHD. Non-ideal MHD has been taken into account by numerous groups (Dapp & Basu 2010; Dapp et al. 2012; Inutsuka 2012; Li et al. 2014; Hennebelle et al. 2016; Masson et al. 2016; Machida et al. 2016; Wurster et al. 2016, 2019; Wurster & Bate 2019; Zhao et al. 2018). These works found that at least small discs always form. When non-ideal MHD is accounted for, turbulence and misalignment tend to be relatively less important. The resulting disc however depends on the magnetic resistivities (Wurster et al. 2018; Zhao et al. 2018) which depend on the grain distribution and cosmic-ray ionisation (Padovani et al. 2013). It has also been found that the Hall effect may introduce a dependence on the respective direction between the magnetic field and the rotation axis (Tsukamoto et al. 2017) but large uncertainties both on the resistivities (Zhao et al. 2016) and the numerical scheme (Marchand et al. 2018) remain.

Another important issue in the collapse calculations are the sink particles used to mimic the stars. These Lagrangian particles accrete the surrounding gas and interact through self-gravity with the whole flow in the simulations. Sink particle parameters such as their accretion radius or the criteria prevailing to their introduction, are not easily justified and remain largely empirical. However previous authors (Machida et al. 2014; Vorobyov et al. 2019) report strong dependence of the resulting disc on the parameters which control the sink particles, particularly the parameters that control the gas accretion.

In an attempt to provide a generic description of disc size in non-ideal MHD calculations, Hennebelle et al. (2016) proposed an analytical approach to infer the disc radius. The calculation is based on simple timescale estimates at the edge of the cloud. Essentially, it is required that the braking and rotation times should be comparable as well as the diffusion and magnetic generation times. This leads to a simple prediction that is recalled later in the paper (Eq. (12)), which has been found to be in reasonable agreement with a set of 3D simulations. A particularly important prediction of this study is that the disc radius, is not expected to vary much with the cloud initial parameters such as its magnetization and rotation (provide they are not too low). In the present paper, we pursue our investigation of disc formation along two lines. First we include sink particles as they were not considered in our previous studies (Hennebelle et al. 2016; Masson et al. 2016) and second we vary more extensively the initial conditions. Importantly, we look in details into the disc properties and show that the accretion rate on the central region is an important parameter which largely contribute to determine the mass, and to a lower extent the radius, of the disc.

In the second section the numerical method as well as the initial conditions used in this work are presented. In the third section, we present in details the result of a run that we use as a reference through the paper and with which other runs will be compared. In the fourth section, we perform a series of runs to carefully investigate the influence of the numerical parameters such as the spatial resolution and the accretion scheme onto the central object. Fifth section presents a systematic investigation of the role of the initial conditions. The influence of the core initial rotation, turbulence, misalignment and magnetisation are all discussed. Finally section six concludes the paper.

2. Setup and simulations

The simulations presented here used the same physical and numerical setup than the ones presented in Hennebelle et al. (2016) and Masson et al. (2016) but for the usage of the sink particles. They also explore a broader range of parameters.

2.1. Code, physics and resolution

To perform our simulations, we used the adaptive mesh refinement code, Ramses (Teyssier 2002), which solves the MHD equations using the finite volume method (Fromang et al. 2006) and maintain the nullity of ∇B within machine accuracy thanks to the usage of the constraint transport method. Periodic boundary conditions are employed. The ambipolar diffusion is treated following the implementation of Masson et al. (2012), which is a simple explicit scheme. The main difficulty is that the timestep associated to the ambipolar diffusion can become very small, particularly in the diffuse gas. To limit this effect, we proceed as in Masson et al. (2016), that is to say we adjust, when required, the ionisation to force the timesteps due to the ambipolar diffusion term to be at least 1/3 of the timestep due to the ideal MHD equations. The method has been tested and results do not sensitively depend on the choice of the threshold (Vaytet et al. 2018).

For the non-ideal MHD coefficient we used the approach presented in Marchand et al. (2016). Only the ambipolar diffusion is being considered. The Ohmic resistivity only becomes important at densities higher than the regime of interest of the present paper and correspondingly at spatial scale smaller than the typical scale described here ($\simeq 10$ AU). The Hall effect is also not considered. A chemical network is solved and the species abundances are tabulated as a function of density and temperature allowing to fastly compute the resistivities within all cells at all timesteps. The assumed ionisation rate is $3 \times 10^{-17} \text{ s}^{-1}$.

To mimic the radiative transfer and the fact that the dust becomes opaque to its own radiation at high density, we use an equation of state (eos) given by

$$T = T_0 \left\{ 1 + \frac{(n/n_{\text{ad}})^{(\gamma_1-1)}}{1 + (n/n_{\text{ad},2})^{(\gamma_1-\gamma_2)}} \right\}, \quad (1)$$

where $T_0 = 10$ K, $n_{\text{ad}} = 10^{10} \text{ cm}^{-3}$, $n_{\text{ad},2} = 3 \times 10^{11} \text{ cm}^{-3}$, $\gamma_1 = 5/3$ and $\gamma_2 = 7/5$. Let us remind that this equation of states mimics the thermal behaviour of the gas, n_{ad} is the density at which the gas becomes opaque to its radiation while $n_{\text{ad},2}$ corresponds to the density at which the H_2 molecules is warm enough for the rotation level to be excited (e.g. Masunaga et al. 1998).

We used the sink particle algorithm developed by Bleuler & Teyssier (2014). The sinks are introduced at a density n_{thres} (our standard value is $n_{\text{thres}} = 3 \times 10^{13} \text{ cm}^{-3}$). Sink particles are placed at the highest refinement level at the peak of clumps whose density is larger than $n_{\text{thres}}/10$.

Further gas is being accreted when the density becomes higher than $n_{\text{acc}} = n_{\text{thres}}/3$ within cells located at a distance less than $4dx$, where dx is the size of the most refined grid, from the sink particle. At each timestep a fraction C_{acc} of this gas ($C_{\text{acc}} = 0.1$ except for one run) is removed from the grid and attributed to the sink. To clarify, at each time step the sink received a mass equal to $C_{\text{acc}} \int (n - n_{\text{acc}}) m_p dV$, where the integral runs over the sink volume. The magnetic field inside the sink particles is not modified and evolves as in the absence of the sink. While this is very simple, this may not be so inaccurate because at small scales, i.e. below 1 AU or so, the magnetic field

becomes poorly coupled to the gas and therefore it is not dragged along with the collapsing gas. The sinks interact with the gas and also between them through their gravitational forces which are directly added to the force exerted by the gas. Inside the sink particles gravitational softening is applied and the gravitational acceleration is given by $GM_*/(r^2 + (2dx)^2)$, where dx is the cell size. Finally, in this work the sinks cannot merge.

The initial resolution is about 256 AU, implying that the cloud diameter is described with 128 cells. Each level of refinement subdivides the cells into two in each of the three dimensions. As the collapse proceeds 7-9 AMR levels are being added to the initial grid which contains $(2^3)^6$ cells and starts at level 6. This provides a maximum resolution in this series of simulations of about 0.5-2 AU. The refinement criterion is the local Jeans length, which is resolved by at least 20 cells.

2.2. Initial condition and runs performed

Two series of runs have been performed. The first one is devoted to exploring the influence of the numerical scheme, in particular the sink particle algorithm, while the second series investigate the influence of initial conditions.

Unlike many works, the simulations are integrated during a relatively long time. This goes from at least 10 kyr after the sink formation to almost 100 kyr for run *R1* and *R2*, for which about 10^7 timesteps have been performed. We can therefore test the evolution of the disc up to the end of the class I phase. Given the small time steps induced by the ambipolar diffusion, the simulations take a lot of time. They have been computed on 40 cores and last several months (2-8).

All cores have a mass equal to $1 M_\odot$, and they have initially a uniform density equal to about $5 \times 10^5 \text{ cm}^{-3}$ and their initial thermal over gravitational energy is equal to 0.4. Outside the core, the density is uniform and equal to this value divided by hundred. This implies that the pressure outside is rather low and therefore the external part of the core undergoes an expansion. The radius of the core is 0.019 pc and the computational box size is four times this value. The cores are in solid-body rotation, which is quantified by the ratio of rotation over gravitational energy, β_{rot} . The magnetic field is initially uniform. Its intensity inside the cylinder that contains the cloud, is constant while its intensity outside this cylinder is also uniform but reduced by a factor $100^{2/3}$. An $m = 2$ density perturbation perpendicular to the rotation axis and equal to 10% has been added to break axisymmetry.

2.2.1. Numerically motivated runs

To understand the effect of the sink particle algorithm and the numerical resolution, we perform 9 runs which are summarized in Table 1. Run *R2*, which will serve as a reference model and is presented in great details below, has an initial mass-to-flux over critical mass-to-flux ratio, $\mu^{-1} = 0.3$ (as in Masson et al. (2016)), we follow the definition of Mouschovias & Spitzer (1976)), implying that it is significantly magnetized but clearly supercritical. The magnetic field axis is along the z-axis and the rotation axis is initially tilted by an angle of 30° with respect to it. It has $\beta_{\text{rot}} = 0.04$. This run is integrated during 100 kyr after the formation of the sink particle.

All runs start with the same initial conditions than run *R2*. Run *R2ns* has no sink particle, while run *R2hsink* uses a density threshold, $n_{\text{thres}} = 1.2 \times 10^{14} \text{ cm}^{-3}$ implying that the sink forms later and accretes gas at higher densities than run *R2*. This allows

Name	l_{max}	$n_{\text{thres}} = 3n_{\text{acc}}$	R_{sink} (AU)	C_{acc}	rest
<i>R2ns</i>	14	NA	NA	NA	no
<i>R2</i>	14	3×10^{13}	4	0.1	no
<i>R2hsink</i>	14	1.2×10^{14}	4	0.1	no
<i>R2lowr</i>	13	3×10^{13}	8	0.1	no
<i>R2lowr1sink</i>	13	3×10^{12}	8	0.1	no
<i>R2r</i>	15	3×10^{13}	2	0.1	no
<i>R2rlowacc</i>	15	3×10^{13}	2	0.01	no
<i>R2rr</i>	15	3×10^{13}	2	0.1	yes
<i>R2rrhsink</i>	15	3×10^{14}	2	0.1	yes

Table 1. Summary of the numerically motivated runs performed. l_{max} is the maximum level of grid used, $l_{\text{max}} = 14$ corresponds to about 1 AU of resolution, $l_{\text{max}} = 13$ to 2 AU and $l_{\text{max}} = 15$ to 0.5 AU. n_{thres} is the density at which the sink particles are introduced while n_{acc} is the density above which the gas is being accreted in the sink, R_{sink} is the sink radius, C_{acc} is the fraction of the gas mass above this density threshold and inside the sink radii which is accreted in a timestep. The parameter rest indicates whether the run uses an output of run *R2* as starting point or is performed from $t = 0$.

Name	μ^{-1}	β_{rot}	θ	\mathcal{M}
<i>R1</i>	0.3	0.01	30°	0
<i>R2</i>	0.3	0.04	30°	0
<i>R3</i>	0.1	0.04	30°	0
<i>R4</i>	0.15	0.04	30°	0
<i>R5</i>	0.07	0.04	30°	0
<i>R6</i>	0.3	0.01	30°	1
<i>R7</i>	0.3	0.04	90°	0
<i>R8</i>	0.15	0.01	30°	1
<i>R9</i>	0.1	0.04	90°	0
<i>R10</i>	0.3	0.0025	30°	0

Table 2. Summary of the physically motivated runs performed. μ is the mass to flux ratio normalised to the critical value, β_{rot} is the ratio of rotation over gravitational energy, θ is the initial angle between the magnetic field and the rotation axis, while \mathcal{M} is the initial Mach number.

us to test the influence of n_{thres} and n_{acc} , which as we see later are crucial. Runs *R2lowr* and *R2lowr1sink* have a lower resolution and two different values of n_{thres} , namely 3×10^{13} and $3 \times 10^{12} \text{ cm}^{-3}$. Runs *R2r* and *R2rlowacc* have a higher spatial resolution and two values of C_{acc} , namely 0.1 and 0.01. With these two runs we can determine whether another accretion scheme influences the disc properties. Finally runs *R2rr* and *R2rrhsink* restart from run *R2* output. They have higher resolution and two different values of n_{thres} . With these two runs we can distinguish the influence of the sink creation and the accretion scheme.

2.2.2. Physically motivated runs

We performed 10 runs in total with the aim of sufficiently exploring the influence of initial conditions. They are summarized in Table 2. For all these runs, 8 levels of AMR are used and $n_{\text{thres}} = 3n_{\text{acc}} = 3 \times 10^{13} \text{ cm}^{-3}$.

We remind that run *R2* is the reference run. Runs *R1* and *R10* have a low rotation with respectively $\beta_{\text{rot}} = 0.01$ and $\beta_{\text{rot}} = 0.0025$. They aim at testing the importance of rotation, which is found to play a weak role. With runs *R3*, *R4* and *R5* we study the influence of the magnetisation, which is the most critical parameter, when the magnetic field is weak. Runs *R6* and *R8*

present on top of a weak rotation a turbulent velocity field which leads to a rms Mach number of 1 initially. Finally, for runs *R7* and *R9* the magnetic field and rotation axis are initially perpendicular.

2.3. Disc identification

We are primarily interested here by the disc formation and evolution and it is therefore essential to define it. We proceed in several steps. First, we apply a density criterion selecting only gas denser than 10^8 cm^{-3} . We then select the cells for which the radial velocity with respect to the sink particle is smaller than half the azimuthal velocity. This defines an ensemble of cells whose mass is well defined. Determining the disc radius is however more difficult because, the discs while reasonably well defined, present nevertheless large fluctuations and generally are not fully axisymmetric. We proceed as follows. First, we determine the mean angular momentum direction of the disc. We then project the disc cell coordinates in the disc plane. We then subdivide the disc plane in 50 angular bins. For each of them we determine the most distant cell, that gives the radius of this angular bin. We then calculate the mean radius, R_{mean} by taking the mean value of the 50 radius obtained for each angular bin and the maximum radius, R_{max} , of the 50 angular bins.

Note that in the study of Joos et al. (2012), more criteria were used. The reason is that in their calculations, ideal MHD was employed and no sink particle was used. Indeed, both tend to produce smoother discs, which are easier to define. Ambipolar diffusion dissipates motions and sink particles make the discs much less massive and therefore less prone to gravitational instabilities. Another difference comes from the outflow cavities and their boundaries which are denser in the ideal MHD case and tend to be picked by simple disc criteria.

3. Detailed description of a reference model

We start with a detailed description of run *R2*.

3.1. Qualitative description

Figure 1 displays the column density for a series of snapshots. To show the disc structure and its close environment, in the left column, the box size is about 100 AU. In the right column, the box size is about 500 AU, allowing to display the larger scales surrounding the disc. Note that the sink particle forms right in the middle of the box. The origin of the x and y coordinates is taken at the left bottom corner of the computational box.

The first snapshot of the left column reveals that initially the disc is highly non-axisymmetric with a prominent spiral arm. It however quickly (i.e. in a few kyr) relaxes in a nearly symmetric object whose radius is on the order of 10 AU. The third and fourth panels show that at later times, the disc grows in size. At time 0.113 Myr, its radius is about 25 AU while at time 0.153 Myr (fourth panel of right column), it is about 100 AU. At all times, dense filaments are connected to the disc and bring further material from the envelope. This anisotropic accretion maintains a certain degree of asymmetry within the disc, that as we can see is never perfectly circular. At some snapshots, see for example time 0.134 (third snapshot of right column), the disc is highly excentric. Another important aspect is that the disc position changes with time. Between the first and the fourth snapshot, it has moved of about 200 AU. Since the initial conditions

of run *R2* are axisymmetric, this implies that symmetry breaking occurs.

A symmetry breaking is indeed clearly visible on the first panel of right column where a loop of dense material has developed in the vicinity of the disc. Inside the loop, the density is much lower. This is a consequence of the interchange instability as described in Krasnopolsky et al. (2012) (see also Joos et al. 2012), which is essentially a Rayleigh-Taylor instability produced by the excess of magnetic flux that has been accumulated in the central region due to the collapse. It typically happens when the flux trapped within the dense gas diffuses out and prevent further accretion to occur. The interchange instability leads to strong instability as seen in the first and second panel of the right column. Not only the loop itself develops in one direction and not isotropically but also because of gravity, Rayleigh-Taylor fingers develop and fall back onto the sink.

3.2. Disc global evolution

Figure 2 shows various relevant quantities integrated over the disc, i.e. its mass, radius, mean density and mean magnetic intensity as a function of time.

In the top panel, the sink mass, M_* , is also given (red curve). The sink is introduced at 0.06 Myr and in about 20 kyr its mass grows to about $0.3 M_\odot$. Apart from a steep drop at early time where the disc is not well defined, M_d stays remarkably constant along time to a value of about $1.5 \times 10^{-2} M_\odot$. This implies that the disc mass over star mass keeps decreasing and typically goes from about 1/10 to 1/30.

Second panel displays the disc radius, blue curve is the mean value, R_{mean} (see Section 2.3) while black is the maximum value, R_{max} . Both values follow the same trend except for some fluctuations of R_{max} , which are due to the difficulty to exclude the filaments that connect to the disc (see Fig. 1). Therefore we adopt R_{mean} as the disc radius. At sink age 10 kyr, i.e. at time 0.07 Myr, its value is about 20 AU. It then grows with time and after 100 kyr reaches roughly 100 AU in size (see right bottom panel). As discussed in Section 5.6, this behaviour turns out to be in good agreement with the analytical prediction of Hennebelle et al. (2016). In particular the growth of the disc radius is proportional to $(M_* + M_d)^{1/3} \approx M_*^{1/3}$.

Third and fourth panels show the mean density and volume averaged magnetic field through the disc (the mean value of all disc cells is taken). Within 100 kyr, the density has decreased by almost 2 orders of magnitude, while the magnetic intensity drops by about a factor of 10. This is broadly consistent with the fact that the mean magnetic field is given by the value in the disc outer part, which itself is close to the envelope value where typically $B \propto n^{1/2}$.

3.3. Disc spatial structure

To better understand and characterize the disc, we now examine left panels of Fig. 3 which portray the mean radial profiles of the column density (top panel), the density (second panel) and several velocities at various timesteps. The density and the velocities are the mean values of cells located below one scale-height, $h \approx r \times C_s / v_{\text{Kepl}}$ and belonging to concentric corona, where v_{Kepl} is the Keplerian velocity and C_s is the sound speed. In the inner part we see that the column density follow a powerlaw, $N \propto r^{-\alpha}$, with $\alpha \approx 0.5 - 1$. The density presents an exponent that is slightly stiffer, particularly within the inner 5 AU and which is about $\approx 1 - 1.5$. Extrapolating the density curves which go up to two AU

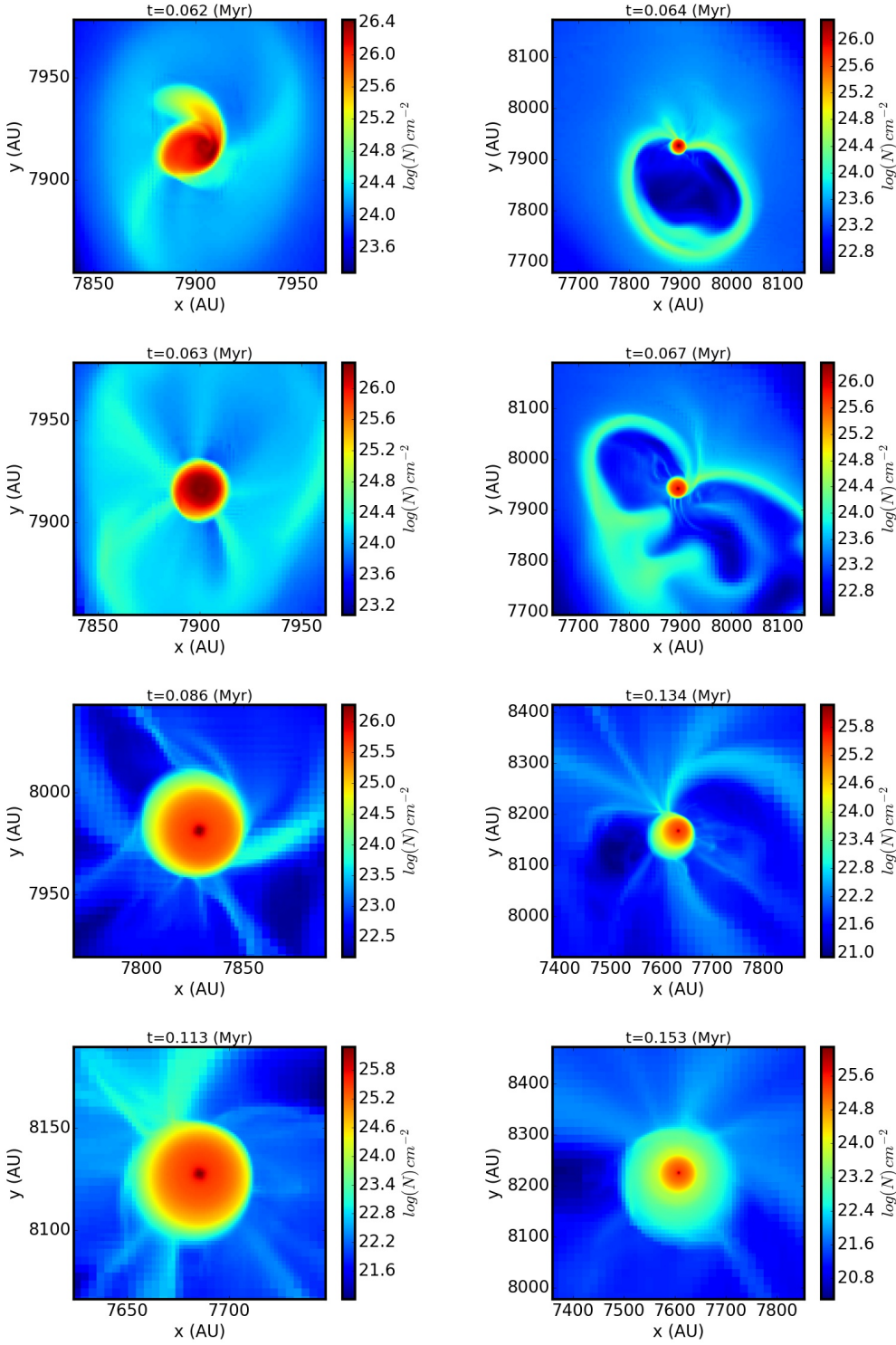


Fig. 1. Column density of run *R2* at several snapshots and two scales. Left: box length is about 100 AU, right: box length is about 500 AU.

(below which concentric corona are not well defined), we see that the central value of the gas density is about 10^{13} cm^{-3} at 1 AU, which is the threshold used for accretion onto the sink particles. This value slowly diminishes as time goes on. At r about 20 AU, a change in the density profile occurs and it becomes much steeper particularly at early times (i.e. $t = 0.086$ and $t = 0.113$ Myr). This corresponds to the position of the accretion shock as revealed by the radial velocity profile displayed in the third panel. At later times ($t = 0.134$ and $t = 0.153$ Myr),

the accretion shock moves away as the disc grows in size. At time $t = 0.153$ Myr, it is located at about 100 AU for instance (see for example the change of the rotation velocity at 100 AU in the left-bottom panel). We see however that a break in the column density and density profile remains around 20 AU. Above this radius, the disc presents a steeper profile which is broadly $\propto r^{-3}$ in column density and $\propto r^{-4}$ in density. Outside the disc, the envelope presents an r^{-2} density profile which is close to the

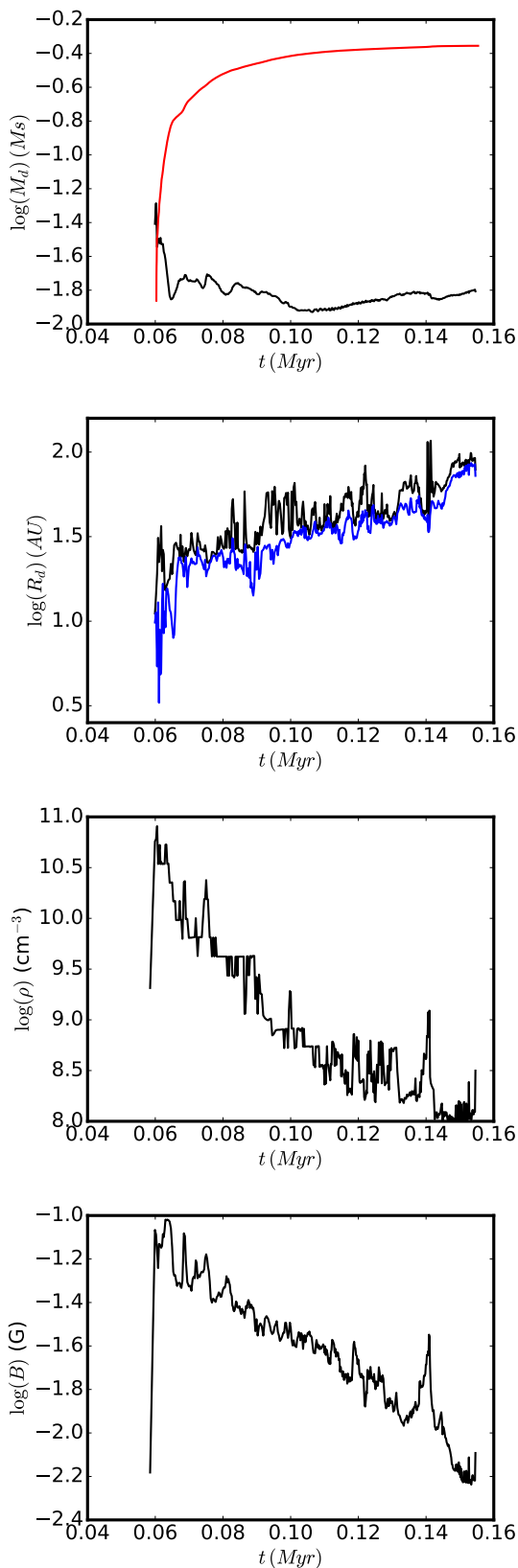


Fig. 2. Global properties of the disc of run R2 as a function of time. Top panel: disc mass (black line) and red line (sink mass). Second panel: disc radius (maximum radius: black line, mean radius: blue line, see Section 2.3). Third panel: mean gas density within the disc. Fourth panel: mean magnetic intensity of the disc.

singular isothermal sphere (Shu 1977) at early times and 10-100 lower at later ones.

The third and fourth panels display the Keplerian velocity, v_{Kep} , the azimuthal gas velocity, v_ϕ , the sound speed, C_s , the Alfvén speed, v_a , and the radial velocity, v_r . Several important features are to be noticed:

- inside the disc, $v_\phi \simeq v_{\text{Kep}}$ except below 3 AU due to the gravitational potential softening. This confirms that the material in the disc is centrifugally supported.
- Outside the disc, v_ϕ drops by a factor of about 10 below v_{Kep} .
- Inside the disc, v_a is about 10 times lower than C_s and 100 times lower than v_{Kep} .
- At the edge of the disc, v_a increases (steeply at early times and more gradually at later ones) and it dominates over the other velocities becoming comparable to the radial one, v_r .
- The radial velocity in the disc inner part is negative and on the order of $C_s/100 - C_s/10$ between 3 and 10 AU (at smaller radius numerical resolution becomes insufficient). At intermediate radius, i.e. between 10-20 AU at time 0.086 Myr and 10-80 AU at time 0.153 Myr, the velocity is globally positive and presents significant fluctuations. In the outer part, above the accretion shock, it is negative and about 10 times C_s .

Two main aspects are of particular importance. First, the value of v_a which is low inside the disc and high outside, indicates that the magnetic field is likely playing an important role in setting the disc radius most likely because strong magnetic braking occurs there (see Section 5.6).

Second we see that the mass flux is obviously not constant through the disc mid-plane since v_r even becomes positive. Clearly to satisfy mass conservation, since the disc column density is nearly stationary in the inner part, mass must flow from higher altitudes. This point is carefully addressed in Lee et al. (submitted) where complementary high resolution radiative calculations are presented.

3.4. Structure of the magnetic field

Since magnetic field is believed to play an important role in the disc by inducing transport of angular momentum through either magneto-rotational instability or magnetic braking, but also possibly by creating structures such as rings (Béthune et al. 2017; Suriano et al. 2018), we look more closely into its structure.

Right panels of Fig. 3 displays the value of β_{mag} as a function of radius for several timesteps as well as the mean radial profiles of B_z , B_r and B_ϕ at three snapshots. The profiles of β_{mag} reveal that while at early times the transition between $\beta_{\text{mag}} > 1$ and $\beta_{\text{mag}} < 1$ occurs through the shock, it is not the case at later times, where the disc outer part is significantly magnetized and present β_{mag} values < 1 .

At time 0.086 Myr B_z and B_ϕ have comparable amplitudes and dominate over B_r . At times 0.134 and 0.153 Myr, B_z decreases and diffuses out of the disc while on the contrary the toroidal field grows in the disc outer part (i.e. between 20 and 100 AU). This growth of the toroidal field occurs in a region where $\beta_{\text{mag}} < 1$ and therefore where the field and the gas are well coupled. It is a natural consequence of the differential rotation (see for example Hennebelle & Teyssier 2008). As can be seen in the fourth left panel of Fig. 3, v_a is larger than C_s in the disc outer part. This excess of magnetic toroidal pressure leads to inflated disc as observed in the third panel of Fig. B.1.

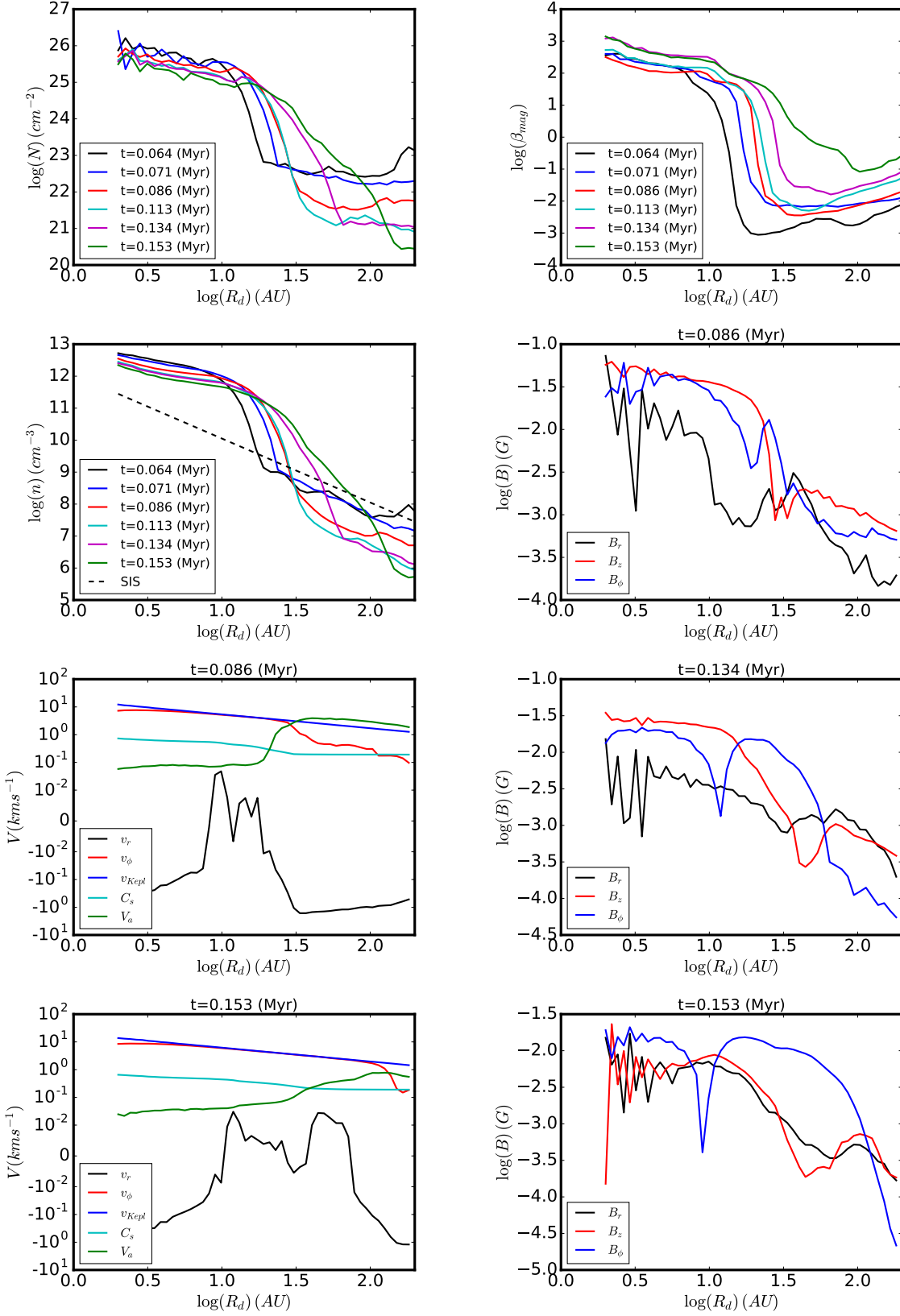


Fig. 3. Radial structure of the disc and surrounding envelope. Top left row: mean column density of the disc of run R2 as a function of radius. Second left panel: mean density of the disc vs radius. Third and fourth left panels: various velocities vs radius within the disc equatorial plane. Top right panel: $\beta_{\text{mag}} = P_{\text{therm}}/P_{\text{mag}}$ as a function of radius within the disc for several timesteps of run R2. Second, third and fourth right panels display for three snapshot, the mean radial, axial and toroidal magnetic field as a function of radius. As can be seen while at early time, the axis field, B_z , is the dominant component, at later time it is the toroidal field which dominates.

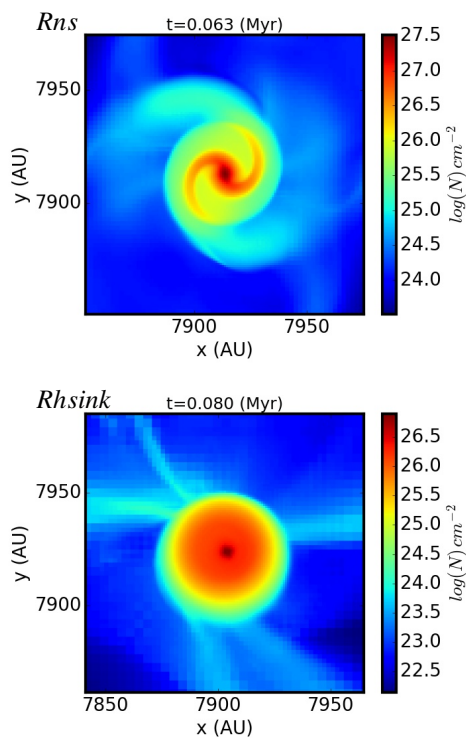


Fig. 4. Column density of run *R2ns* (top) and run *R2hsink* (bottom). These runs are identical to the reference run *R2* but *R2ns* has no sink particle while *R2hsink* has a value n_{acc} which is 4 times higher. They should be compared with Fig. 1. In the absence of sink particles the disc is more extended due to prominent spiral patterns. With a higher value of n_{acc} the disc is also a bit bigger and more massive (see Fig. 5) than the disc in run *R2*.

4. Influence of sink particles on disc evolution

To understand disc formation, it is necessary to use sink particles. How the sink particles are exactly implemented remains largely arbitrary and it is necessary to understand the effect of the sink algorithm on the disc properties.

4.1. Disc evolution without sink particle

To see the drastic influence of sink particles, the top panel of Fig. 4 portrays the column density of run *R2ns* in which no sink particle is being used. The comparison with Fig. 1 shows drastic differences. Clearly the disc is larger and presents prominent spiral patterns. These later are largely a consequence of the fact that in the absence of sink particle, the gas that has accumulated in the central, thermally supported hydrostatic core may be transported back at larger radii and contribute to make the disc gravitationally unstable. Sink particles on the other hand introduce a strong irreversibility mimicking gas accretion onto stars. Clearly runs that do not use sink particles are not sufficiently realistic to describe the long time disc evolution. As we show below, the question however of which sink parameters should be used and how the gas is retrieved from the grid are crucial.

4.2. Influence of sink parameters on sink mass evolution

Top panel of Fig. 5 shows the sink mass (dashed lines) as a function of time for the numerically motivated runs (Table 1). In this series of runs, the numerical resolution varies by a factor 4 and

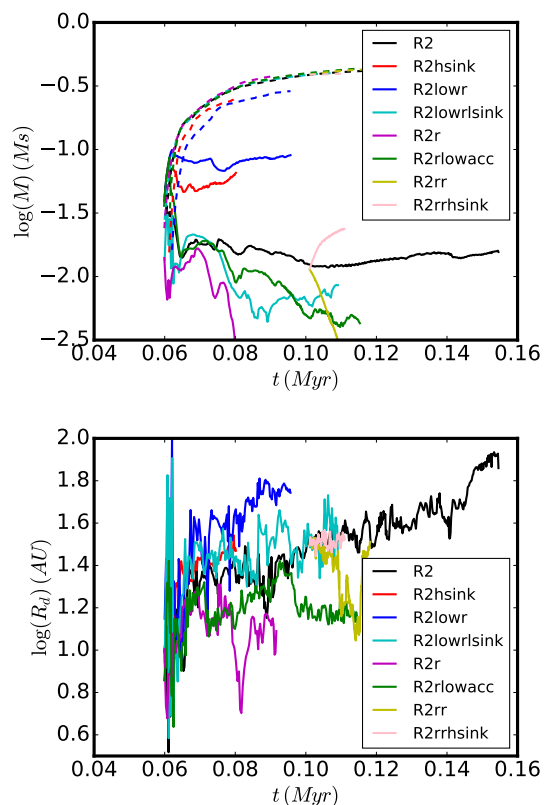


Fig. 5. Comparison between disc radius and mass for the 9 numerically motivated runs listed in Table 1. In top panel the dashed lines represent the mass of the sink particles. While the sink mass does not depend significantly on the detailed of the numerical algorithm (i.e. sink threshold and resolution), the disc properties depend very much on it.

the sink accretion threshold by a factor 40. Clearly, the sink mass evolution is only marginally influenced by the numerical parameters. In all runs the sinks formed roughly at the same time and the mass evolution is very similar.

This is an important conclusion because it confirms that the global evolution of the dense core is not very much affected by the numerical algorithm. In particular, the accretion rate onto the sink particles is likely a consequence of the large scale of the core rather than the detailed small scale processes. In other words, the traditional picture that the infalling gas is stored in the centrifugally supported disc and then gets transported through it up to the star, is not supported by the present simulations, at least in its simplest form.

4.3. Influence of sink parameters on disc evolution

To understand the influence of the sink parameter, run *R2hsink*, which has a value of n_{acc} 4 times above the one used in run *R2*, has been carried out. Bottom panel of Fig. 4 shows the disc of run *R2hsink* at time 0.08 Myr. As can be seen from a comparison with Fig. 1, the disc of run *R2* and *R2hsink* are similar but the latter is more massive and slightly bigger. The reason is simply that the central disc density is higher for run *R2hsink* because of the higher value of n_{acc} .

Top panel of Fig. 5 portrays the disc mass (solid lines) evolution while bottom panel displays the disc radius for all runs listed in Table 1. Very large variations are observed. For instance the disc mass varies by more than one order of magnitude be-

tween runs *R2lowr* and runs *R2r*. This indicates that unlike for the sink mass, the disc mass and, to a lower extent, the disc radius very much depend on the numerical scheme. Below we analyse in details the various runs but two conclusions can already be drawn. First of all, the disc itself does not determine the accretion onto the star in the sense that varying the mass of the disc does not necessarily affect the accretion onto the star. Second of all, the disc properties, in particular its mass, cannot be reliably predicted because they are controlled by numerical parameters.

4.3.1. Interdependence between resolution and sink particle threshold

First, we compare runs *R2* and *R2hsink*. The only difference is the value of n_{acc} , which is 4 times larger for *R2hsink* than for *R2*. The mass of the disc is about ≈ 3 times larger in run *R2hsink* while the disc radius is comparable though slightly larger. The reason is simply that as for run *R2* (see Figs. 3 and A.1), the density at the edge of the sink particle is determined by n_{acc} and since the profile is similar, the mass is almost proportional to n_{acc} .

Second, we compare runs *R2*, *R2lowr* and *R2r*. These three runs have same value of n_{acc} but differ in spatial resolution, which go from 2 AU (*R2lowr*) to 0.5 AU (*R2r*). The differences between the three discs are rather large, with a factor of ≈ 3 -5 difference between the disc mass of runs *R2lowr*, *R2* and *R2r* respectively. In terms of radius, it is a factor of 2-3. This clearly indicates that both the resolution and the sink density threshold, n_{acc} , are important in determining the disc properties. This is confirmed by run *R2lowr* which has a resolution of 2 AU and a value $n_{\text{acc}} = 10^{12} \text{ cm}^{-3}$, i.e. 10 times below the values in the runs *R2*, *R2lowr* and *R2r*. In this case, the disc mass is inbetween its value in runs *R2* and *R2r*.

Roughly speaking the disc mass is proportional to $dx^{-\delta} n_{\text{thres}}$ with $\delta \approx 1 - 2$. This can simply be understood as an inner boundary conditions. The density at the radius $r = dx$ is equal to $n_{\text{acc}} = n_{\text{thres}}/3$, therefore the density within the disc is about $n(r) \approx n_{\text{acc}}(dx/r)^{\delta'}$ with $\delta' \approx 1 - 1.5$. Thus since the disc density decreases with resolution, the disc mass decreases as well.

4.3.2. Deciphering the role of density threshold and sink creation

To be certain that the effects we are observing is not due to differences of the sink creation time, we have performed two runs, namely *R2rr* and *R2rrhsink*, for which we restart from an output of run *R2*. The two runs have a resolution of 0.5 AU and a threshold density of $n_{\text{acc}} = 10^{13} \text{ cm}^{-3}$ and 10 times this value respectively. We see that the disc mass of run *R2rr* drops by at least a factor of 3 while the one of run *R2rrhsink* increases by about 50% while its radius does not evolve significantly.

This confirms that the observed differences are due to the accretion condition onto the sink particles.

4.3.3. The amount of accreted gas

Finally, to investigate whether the disc mass is indeed influenced by the accretion rate from the disc onto the star, we performed run *R2r* which is identical to run *R2r* except that the value of C_{acc} is 0.01 instead of 0.1. We recall that this is the fraction of gas above n_{thres} which is accreted at all timesteps.

Figure 5 shows that the disc of run *R2r* is more massive (up to 3-4 times depending of the period) and roughly 2

times larger in radii. This confirms that the accretion rate at the inner boundary is a fundamental quantity that drastically impacts the disc properties, in particular its mass.

4.4. Physical interpretation

The results presented in Fig. 5 demonstrate that the accretion onto the sink particle, which operates as an inner boundary condition, is a major issue for the disc. Similar results have been obtained by Machida et al. (2014) and recently by Vorobyov et al. (2019) who found that the accretion rate in their sink particles has a drastic impact onto the disc. The obvious question is then whether this choice is realistic and what physically determines the inner boundary. We propose that this is the star-disc connection which could be limiting the accretion and to illustrate how it may work we propose a simple model suggesting that the choices made here are reasonable. Note that at the T-Tauri stage, it is believed that the accretion proceeds through the magnetospheric accretion process (Bouvier et al. 2007). However our simulations take place far earlier than the T-Tauri phase and also unlike what is assumed in the classical models, we do not find, that most of the accretion proceeds through the bulk of the disc.

We use the classical stationary α -disc model which assumes that the effective disc viscosity is given by

$$\nu = \alpha C_s h = \alpha C_s^2 / \Omega, \quad (2)$$

where h is the scale height, Ω is the Keplerian rotation and α is a dimensionless number on the order of $10^{-3} - 10^{-2}$ depending on the disc physics. It is well known Pringle (e.g. 1981) that the disc surface density, Σ is given by

$$\Sigma = \frac{\dot{M}_d}{3\pi\nu} + \frac{C}{3\pi\sqrt{GM_*\nu}R^{1/2}}, \quad \Sigma = 2\rho h, \quad (3)$$

where \dot{M}_d is the accretion through the disc, M_* is the mass of the central star and C is a constant, which is usually chosen in such a way that at the star radius, R_* , $\Sigma(R_*) = 0$. This choice, while natural, leads to an infinite velocity at R_* since

$$v_{r,d} = \frac{-\dot{M}_d}{2\pi R \Sigma}, \quad (4)$$

and \dot{M}_d is assumed to be constant through the disc.

To illustrate how the connection between the star and the disc, may influence the disc characteristics, we make very simple assumptions. First, we assume that the star is spherical and present a profile of density, ρ_* , temperature T_* and velocity v_* . This latter is not zero because the star is accreting material from the outside at a rate \dot{M}_* , which we assume is nearly spherical. That is to say, the star is assumed to accrete both through the disc and also to receive a nearly spherical flux of gas. Since we are interested by the outer layer at which the disc connects, we have

$$v_{r,*} = \frac{-\dot{M}_*}{4\pi R^2 \rho_*}. \quad (5)$$

Since the fluid velocity and density must be continuous, we have $v_{r,d} = v_{r,*}$ and $\rho_d = \rho_*$, which leads to

$$\frac{\dot{M}_d}{M_*} \approx \frac{h}{2R_*} \approx \frac{C_s}{2R_*\Omega(R_*)}. \quad (6)$$

At early stage, the stellar radius is typically a few solar radii and the temperature of the gas on the verge to enter the star is

about 10^4 K (Masunaga & Inutsuka 2000; Vaytet et al. 2018). We estimate

$$\frac{\dot{M}_d}{\dot{M}_*} \simeq 10^{-2} \left(\frac{T_d}{10^4 \text{ K}} \right)^{1/2} \left(\frac{M_*}{M_\odot} \right)^{-1/2} \left(\frac{R_*}{R_\odot} \right)^{1/2}, \quad (7)$$

which shows that under these circumstances, the accretion rate through the disc is a few percent of the accretion onto the star. In the context of an α -disc, this also fixes the column density profile.

We stress that the present model is essentially illustrative and that a more detailed analysis should be performed. Other assumptions will lead to different disc properties. It however supports the idea that the accretion rate through the disc and its density profile, at large scale, may be influenced by the small scale star-disc connection at the early stage of the star formation process. Unfortunately little is presently known on this phase as studies which have addressed the second collapse and the formation of the protostar itself (e.g. Machida et al. 2006; Tomida et al. 2013; Vaytet et al. 2018) are very limited in time due to the small Courant conditions.

4.5. A criteria for sink accretion threshold

The obvious question is therefore what value of the accretion threshold should be used. As discussed in the previous section, this is not an easy question as it may request a detailed knowledge of the disc structure at small radii may be up to the star itself. To proceed we again use the standard α -disc model. Using Eqs. (2-3) we get

$$\rho \simeq \frac{\Sigma}{2h} = \frac{\dot{M}_d}{6\pi\alpha C_s h^2} = \frac{\dot{M}_d \Omega^2}{6\pi\alpha C_s^3}, \quad (8)$$

Now with Eq. (1), we have when $n \gg n_{ad}$:

$$C_s \simeq C_s^0 n^{2/10} n_{ad}^{-2/6} n_{ad,2}^{5/6-7/10}, \quad (9)$$

where C_s^0 is the sound speed in the isothermal envelope and is about 0.2 km s^{-1} , and this leads for the gas density to

$$n(R) \simeq \left(\frac{G\dot{M}_d M_*}{6\pi\alpha m_p} (C_s^0)^{-3} n_{ad} n_{ad,2}^{-2/5} R^{-3} \right)^{5/8}, \quad (10)$$

where m_p is the mean mass per particle and $n = \rho/m_p$. We therefore obtain

$$n(R) \simeq 5.5 \times 10^{13} \text{ cm}^{-3} \left(\frac{\dot{M}_d}{10^{-7} M_\odot \text{ yr}^{-1}} \right)^{5/8} \left(\frac{M_*}{1 M_\odot} \right)^{5/8} \left(\frac{\alpha}{0.01} \right)^{-5/8} \left(\frac{R}{1 \text{ AU}} \right)^{-15/8}. \quad (11)$$

Several points must be discussed. First the typical value of n at 1 AU is expected to be around 10^{13} cm^{-3} if $M_* = 0.3 M_\odot$ as it is the case in the present study. Second this density depends on the accretion rate through the disc as well as the effective viscosity. Both are heavily uncertain and their estimate requires a careful and specific investigation. The reference value $\dot{M}_d = 10^{-7} M_\odot \text{ yr}^{-1}$, is simply based on Eq. (7) and on the measured accretion ratio in the sink which is on the order of $10^{-6} - 10^{-5} M_\odot \text{ yr}^{-1}$.

When using the sink particles, one must make sure that the density at which the gas is accreted within the sink is close to the value stated by Eq. (11). There is however another source of uncertainty which comes from the radius at which this should be evaluated. Typically, it could be either the sink radius, $4dx$, or

the resolution, dx . As revealed by Fig. 3, the density reached n_{acc} only in the very center. Therefore estimating n_{acc} at dx seems to be a better choice. In any case, there is, as described in the present section, a dependence of the accretion threshold n_{acc} into the resolution. Typically from Eq. (11), it broadly scales as dx^{-2} , which is compatible with what as been inferred from the numerical experiments presented above. Finally, we stress that in reality the value of n_{acc} should be time dependent as it depends on M_* and \dot{M}_d , which both evolve with time. It is also possibly physics dependent since it depends on α , which in turn may depend on the magnetic intensity for instance.

5. Influence of initial conditions on disc formation and evolution

We now investigate the influence that initial conditions have onto the disc evolution. We focus on the global disc properties, i.e. its mass and size. As discussed in the previous section, the accretion threshold n_{acc} is of primary importance while highly uncertain. We adopt the value $n_{acc} = 10^{13} \text{ cm}^{-3}$ as it is close to our analytical estimate. While it is likely that better, time-dependent, estimates will have to be used in the future, it is nevertheless important to investigate the influence of initial conditions because they are also playing an important role in the disc evolution. In particular, the resulting discs can be compared to understand the consequences of the various processes. From the previous section, we saw that the mass of the disc is nearly proportional to n_{acc} , as long as this parameter varies from a factor of a few. So in principle, the results presented below should remain valid for other values of n_{acc} by simply multiplying the disc mass by $n_{acc}/10^{13} \text{ cm}^{-3}$.

5.1. The impact of rotation

Figure 6 displays the disc mass and the disc radius as a function of time for runs R1, R2 and R10 (i.e. $\beta_{rot} = 0.01, 0.04$, and 0.0025 respectively). During the first 50 kyr, there is a clear trend for the disc of run R1 to be about 2 times less massive on average than the disc of run R2 but at time $\approx 0.11 \text{ Myr}$, the two runs present discs of comparable masses. The radius of the two discs are close but there is a clear trend for the disc of run R1 to be slightly smaller by a few tens of percents. With run R10 the situation is a bit more confusing. There is a short phase, between 0.07 and 0.08 Myr during which the disc of run R10 is about 50% smaller and less massive than the disc of run R1. However, passed this phase, the disc of run R10 becomes even slightly bigger and more massive than the disc of run R2. A more detailed analysis reveals that the disc in run R10 becomes very elliptical. Altogether rotation appears to have only a modest influence on the disc characteristics, though obviously very small rotation would certainly lead to major differences.

At first sight this is surprising since the disc radius is proportional to j^2 where j is the angular momentum. Therefore increasing β_{rot} by a factor of 4 may lead to a disc 4 times bigger. This however is not the case because magnetic braking largely controls the formation of disc and is responsible for redistributing the angular momentum through the core. Indeed the analytical expression of the disc radius (Eq. (13) of Hennebelle et al. (2016)) does not entail any dependence on β_{rot} (contrarily to Eq. (14) of Hennebelle et al. (2016)). This is a consequence of magnetic braking and magnetic field generation. A larger rotation leads to a stronger B_ϕ , which in turn leads to more efficient magnetic braking.

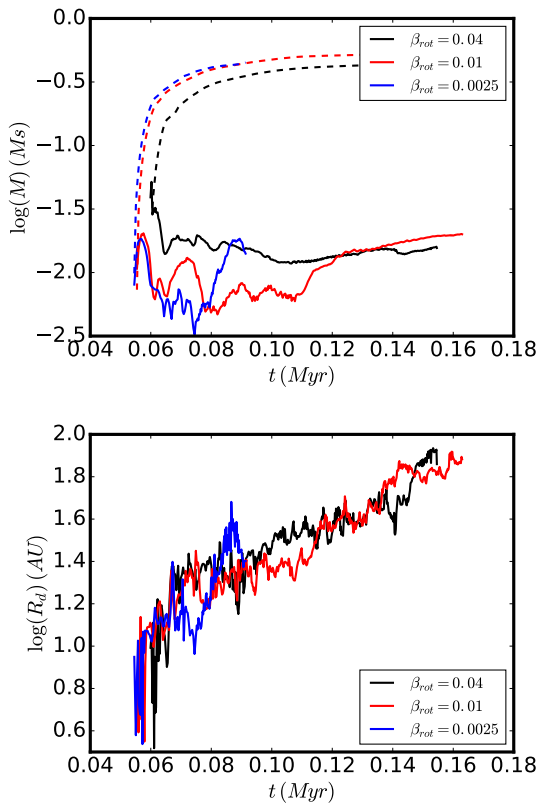


Fig. 6. Comparison between disc mass and radius for runs R1, R2 R10, i.e. having 3 levels of rotation corresponding to $\beta_{\text{rot}} = 0.01$, 0.04, and 0.0025 respectively.

5.2. The impact of magnetic intensity

The magnetic intensity is expected to be a fundamental parameter regarding disc formation and here we investigate four values of μ , going from significantly magnetized (i.e. $\mu^{-1} = 0.3$) to weakly magnetized ($\mu^{-1} = 0.07$). Figure 7 shows the disc at 3 snapshots for runs R3 (left, $\mu^{-1} = 0.1$) and R5 (right, $\mu^{-1} \approx 0.07$). The disc in run R3 is a bit larger than the disc of run R2 and is surrounded by spiral arms whose size is about 200-400 AU, that persist and even grow with time (not shown here for conciseness). There are also prominent spiral arms within the disc itself as shown by the middle and bottom left panel. This is very similar to the disc shown by Tomida et al. (2017).

The disc formed early in run R5 (top right panel) is visibly both massive and large with prominent spiral arms. Further fragments develop through gravitational instability within the arms and a new object forms as seen in bottom-right panel. Two smaller discs form around each of the two stars with radii on the order of 20-40 AU. Around the binary a larger scale rotating structure is seen, which may give rise to a circumbinary disc.

Figure 8 portrays the disc mass and disc radius as a function of time for runs R2, R3 and R4 ($\mu^{-1} = 0.3$, 0.1, and 0.15 respectively, but not run R5 since it fragments). First let us note that the sinks form about 10 kyr later in run R2 than in runs R3 and R4 because of the magnetic support which delays the collapse by about 25% in time. The disc in run R3 is about 5-6 times more massive than the disc of run R2 and it is about 2 times larger (the large fluctuations are due to the spiral arms which continuously evolve). The disc of run R4 is initially a little more massive than the one in run R2 but over time $t = 0.08$ Myr, the mass of the discs of runs R2 and R4 are almost identical. In terms of radius,

the difference is on the order of $\approx 50\%$ until $t = 0.09$ Myr where the two radius become very close.

Altogether these results show that for magnetic fields such that $\mu^{-1} > 0.15$, the magnetic intensity does not influence very strongly the disc properties. For weaker field, typically corresponding to $\mu^{-1} = 0.07 - 0.1$, we see a stronger dependence leading to bigger discs that can possibly fragment. As explained in Hennebelle et al. (2016) this is largely a consequence of the ambipolar diffusion that tends to regulate the magnetic intensity at high density. Note that more variability is reported in Masson et al. (2016) than what is inferred here particularly regarding the cases $\mu = 3$ and $\mu \approx 6$. The difference comes from the sink particles, which are not used in Masson et al. (2016). As shown in Fig. 4, when they are not used strong spiral patterns develop because the gas that has piles up in the centre can expand back forming more massive disc than it should.

5.3. The impact of misalignment

Misalignment has been identified to be playing a significant role in the process of disc formation particularly for values of $\mu > 5$ (Hennebelle & Ciardi 2009; Joos et al. 2012; Li et al. 2013; Gray et al. 2018; Hirano & Machida 2019). Typically it has been found that large discs form more easily in the perpendicular configuration although Tsukamoto et al. (2018) concluded based on an analysis of the amount of angular momentum that this may not be the case when non-ideal MHD is considered. This is however based on the amount of angular momentum available in the dense gas as they do not report about the discs themselves.

Figure 9 shows the disc for runs R7 (left panels) and R9 (right panels) which both have an initial angle between magnetic and rotation axis equal to 90° and a magnetisation of $\mu^{-1} = 0.3$ and $\mu^{-1} = 0.1$, respectively. Both discs have their axis along the x-axis i.e. along the initial rotation axis.

The disc of run R7 is small in size and comparable to the one of run R2. This is confirmed by Fig. 10, which shows that both the mass and the radius are very similar to the one of run R2 with the radius of the latter being a few tens of percent smaller than the former.

The case of larger μ , i.e. runs R3 and R9 is different. From Fig. 9, it is clear that the disc of run R9 is rather large and typically 3 times larger than the disc of run R3. This is also clearly shown by Fig. 10 where it is seen that at the end of the integration, both the mass and the radius of run R9 disc are almost 3 times the ones of run R3 disc. Note that while run R9 is both massive and large, it does not seem to show any sign of fragmentation so far. The reason is likely because it has a stronger field than run R5 for instance.

The conclusion is therefore broadly similar to the one inferred from ideal MHD calculations (Joos et al. 2012), that is to say the orientation does not have a drastic impact for moderate to strong field (i.e. $\mu < 3$), it can make a significant difference for weak magnetisation (in the present case $\mu = 10$). We note nevertheless that in ideal MHD calculations, the influence of the misalignment appears to be important for values as low as $\mu = 3$.

5.4. The impact of turbulence

The impact of turbulence on disc formation has been studied in the context of ideal MHD and it has been found (Santos-Lima et al. 2012; Joos et al. 2013) that it reduces the magnetic flux in the core inner part therefore favouring disc formation. It has also been proposed (Seifried et al. 2013) that it is the disorganised

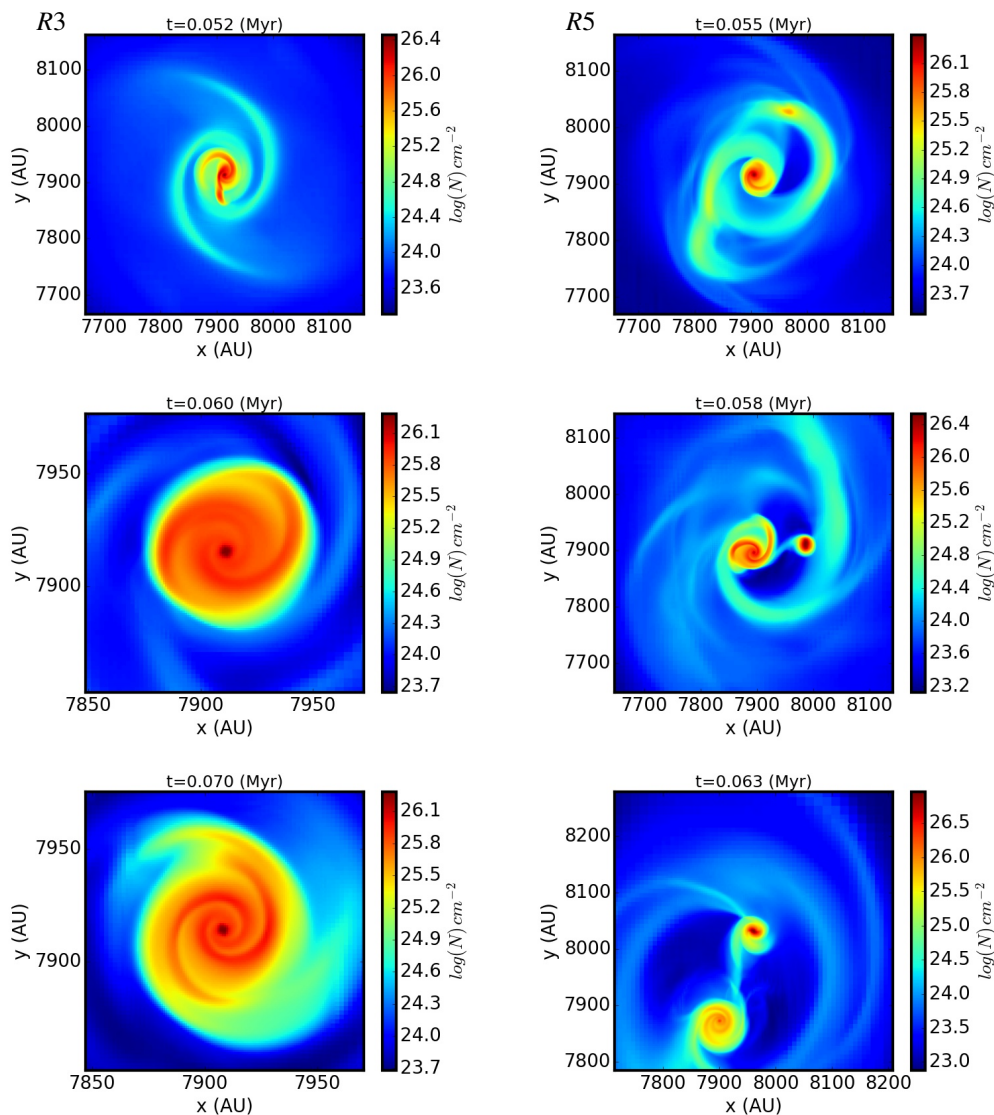


Fig. 7. Column density of runs R3 (left) and R5 (right), i.e. weakly magnetized runs, for two snapshots. For run R3 while the magnetic intensity is 3 times weaker than for run R2, the disc is only marginally larger. Two noticeable differences however are that the disc presents strong and persistent spiral arms and that large scale spiral arms outside the disc also remain. As can be seen, run R5 (which has a magnetic intensity about 4 times lower than run R2) fragments in 2 objects.

structure of the field, induced by turbulence, which reduces the effect of magnetic braking while Gray et al. (2018) concluded that the most important effect of turbulence is the misalignment it induces (see also Joos et al. 2013).

Cases that included both turbulence and ambipolar diffusion have been presented in Hennebelle et al. (2016) and it has been found that the discs were not particularly different from the cases where no turbulence was initially present. Both runs R6 and R8 (which are identical apart for their magnetisation) confirm this conclusion as revealed by Fig. 11 where the disc and radius mass are portrayed for runs R2 ($\mu^{-1} = 0.3$ and no turbulence) and R6 ($\mu^{-1} = 0.3$ with an rms Mach number of 1 initially) as well as runs R4 ($\mu^{-1} = 0.15$ and no turbulence) and R8 ($\mu^{-1} = 0.15$ with an rms Mach number of 1 initially). At early time, disc of run R6 is 50% smaller than for R2 but this may be in part due to the slightly delayed collapse of run R6 with respect to run R2 (a consequence of turbulence) and also to the lower rotation of run R6. After 20 kyr, the discs of runs R2 and R6 have indistinguishable sizes and masses.

We conclude that in the presence of ambipolar diffusion, turbulence does not have a significant impact on the disc. This is likely because ambipolar diffusion has an effect on magnetic field that dominates over the diffusion induced by turbulence. Another complementary effect is the dissipative nature of ambipolar diffusion, which likely tends to reduce turbulence by enhancing its dissipation.

5.5. Magnetic intensity vs density

To interpret the results inferred in this section, the magnetic intensity distribution is of fundamental importance since magnetic braking is largely controlling disc formation. Figure 12 portrays the mean magnetic intensity, B , per logarithmic bin of densities for all runs at time 0.06 Myr. We note that the magnetic field intensity as a function of density does not evolve very significantly with time so the particular choice made here is not consequential.

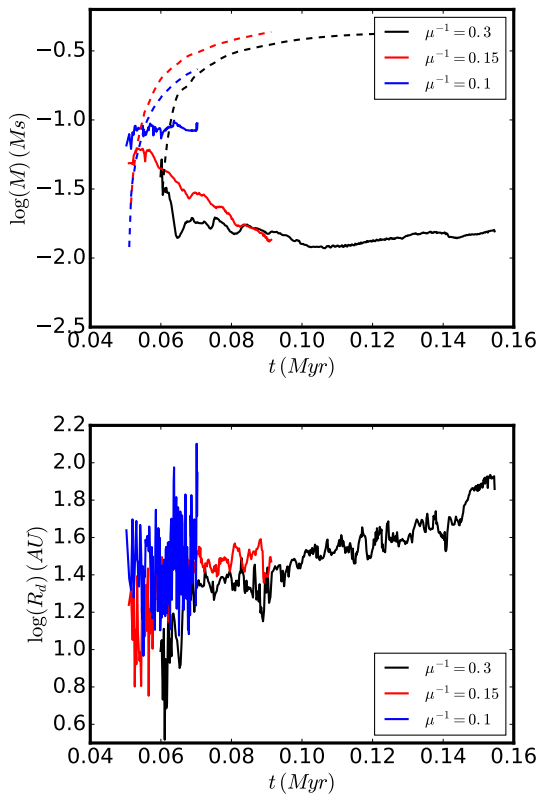


Fig. 8. Comparison between disc mass and radius for runs *R2*, *R3* and *R4*, i.e. having 3 levels of magnetization corresponding to $\mu^{-1} = 0.3$, 0.1 and 0.15 respectively.

In the envelope for densities between 10^4 and 10^8 cm^{-3} , B increases with the density. Some discrepancies are seen between the runs. The most magnetized ones present a more shallow profiles (typically with powerlaw exponents of about 1/2) while for the less magnetized ones, the profiles are stiffer (and more compatible with powerlaw exponents close to 2/3). At higher densities, i.e. 10^8 - 10^{10} cm^{-3} depending of the runs, a plateau of magnetic intensities formed. Its value is nearly the same for all runs, except for runs *R3*, *R5* and *R9* which present lower intensities. The reason of this behaviour (see Hennebelle et al. 2016) is that the ideal MHD holds in the low density envelope while at high density, ambipolar diffusion is dominant and an equilibrium settles between the inwards flux of magnetic field dragged by the collapsing motion and the ambipolar diffusion.

The distribution for run *R9* is particularly intriguing. It has the same initial magnetisation as run *R3*, which is more magnetised than the run *R5*, but the magnetisation at high density in run *R9* is the weakest. On the other hand, we see that it presents an excess compared to the other runs of magnetic intensity around $n \approx 10^6$ cm^{-3} . This strongly suggests that in run *R9* efficient diffusion of the magnetic field occurred. This is probably a consequence of the perpendicular configuration as well as the weak intensity which lead to a strongly wrapped field.

Importantly, we find an obvious qualitative correlation between the size of the disc and the field intensity in the core inner part (i.e. $n > 10^8$ cm^{-3}).

5.6. Comparison between simulation and analytical theory of disc radii

To better understand the physics that governs the disc evolution, we now compare the numerical results presented above with the analytical modelling presented in Hennebelle et al. (2016). Let us remind that this expression is obtained by simply requiring the equality between on one hand the magnetic braking and rotation time and on the other hand, the magnetic diffusion and generation of the toroidal magnetic field at the disc edge. The radius expression is

$$R_{\text{theo}} \approx 18 \text{ AU} \times \delta^{2/9} \left(\frac{\eta_{\text{AD}}}{0.1 \text{ s}} \right)^{2/9} \left(\frac{B_z}{0.1 \text{ G}} \right)^{-4/9} \left(\frac{M_*}{0.1 M_{\odot}} \right)^{1/3}. \quad (12)$$

In this expression, η_{AD} is the magnetic resistivity, B_z is the vertical component of the magnetic field at the edge of the disc and M_* the mass of the star. δ is a coefficient such that $\rho = \delta \rho_{\text{SIS}} (1 + v_{\phi}^2/C_s^2/2)$, where ρ_{SIS} is the density of the singular isothermal sphere. Note that while this expression is reasonable to describe the equatorial density of a rotating hydrodynamical collapsing core, it is not obviously the case in a misaligned magnetized dense core as the densest part of the collapsing envelope, the pseudo-disc, is generally not lying in the plane of the disc (as is particularly obvious from Figs. B.1 and B.2). Moreover as it is clear from Fig. 3, the envelope and the disc are connected through a shock. This suggests that using for the density at the disc edge the expression $\rho = \delta \rho_{\text{SIS}} M^2$ would be more appropriate. However, since $M = v_r/C_s \approx v_{\phi}/C_s$, this leads to exactly the same dependence and leaves Eq. (12) essentially unchanged.

To test this formula, we have measured the mean magnetic intensity in the disc as a function of time. It gives a reasonable proxy for the magnetic field at the edge. The values of η_{AD} and δ are not easy to estimate because the density changes abruptly at the edge of the disc. Fortunately, η_{AD} in this range of parameter does not change too steeply and both parameters come with an exponent 2/9 in Eq. (12). For the sake of simplicity, we therefore keep them constant.

Figure 13 shows the ratio of the measured disc radius to the theoretical expression for the 8 runs (run *R5* is not considered because it fragments) as a function of time. Altogether we see that within a factor of ≈ 2 , we indeed have $R_d \approx R_{\text{theo}}$. Apart for run *R9* and maybe *R3*, there is a general trend for R_{theo} to be about 50% larger, which is probably a consequence of $\eta_{\text{AD}} \approx 0.1$ to be a little too high and more generally to the difficulty in inferring a single value of B_z and of η . For most runs, apart from the large fluctuations at the beginning where the disc is not well settled, R/R_{theo} varies within a factor of about 2. This is similar to what has been inferred in Hennebelle et al. (2016) although since sink particles are used here, the agreement is even better. Compared with the disc radius as a function of time and for different runs (see for instance Fig. 10), it is clear that the ratio R_d/R_{theo} presents much less variability which also illustrates the reasonable validity of Eq. (12). In particular, we see that R_d/R_{theo} does not vary appreciably with time, which indicate that $R_d \propto M^{1/3}$ is a good approximation.

We concluded that altogether the theoretical expression provides the correct answer within a factor of ≈ 2 -3.

6. Conclusion

In this paper we have presented two series of numerical simulations aiming at describing the collapse of a magnetized dense

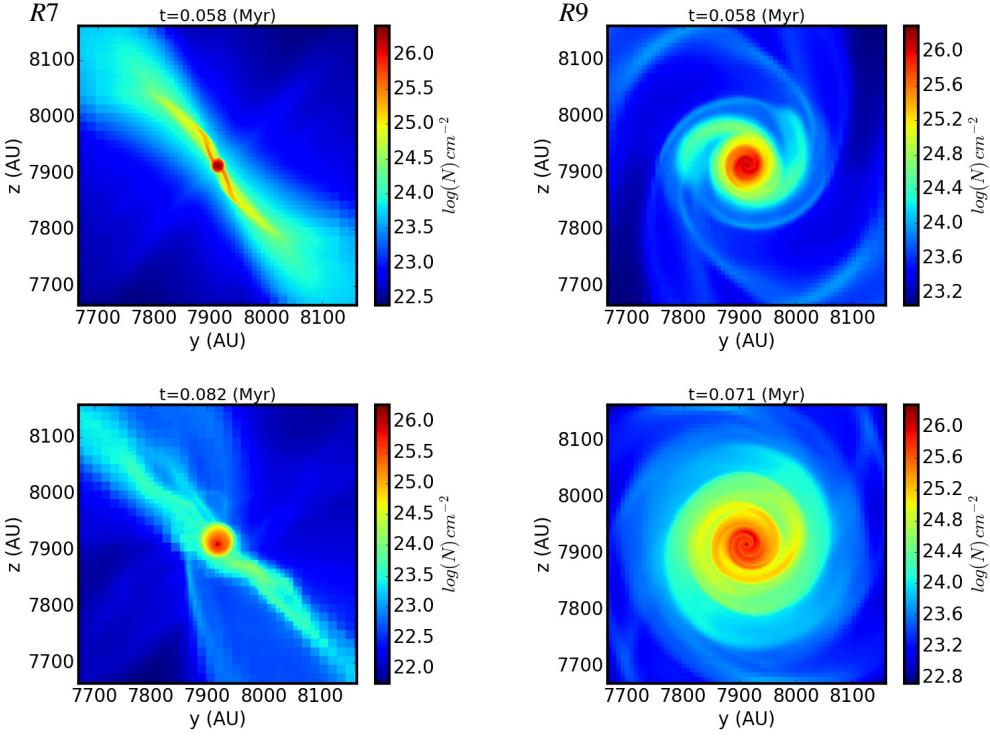


Fig. 9. Column density of runs *R7* (left) and *R9* (right) for two snapshots. Both runs present initially a misalignment between the magnetic and rotation axis of 90° . Run *R7* which has the same magnetic intensity than run *R2*, presents a disc that is rather similar to it. Run *R9* which is 3 times less magnetized than run *R2* (and have the same magnetization than run *R3*), presents a massive and large disc.

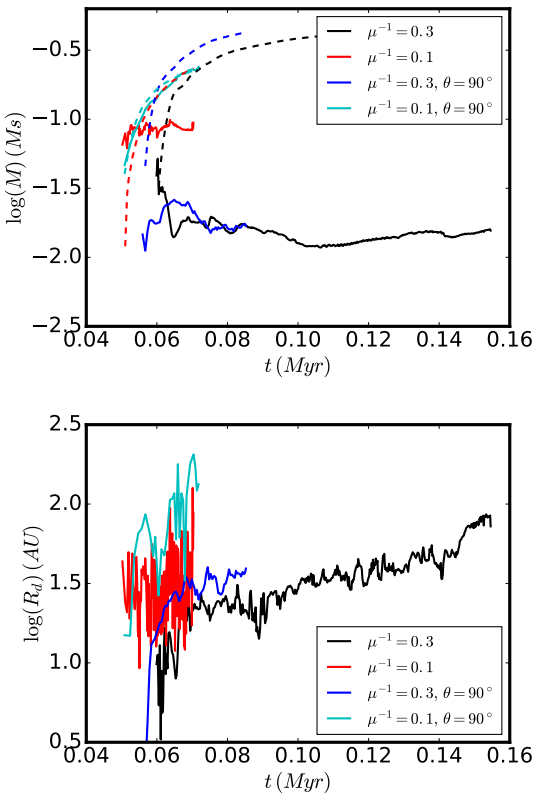


Fig. 10. Comparison between disc radius and mass for runs *R2*, *R3*, *R7* and *R9*, i.e. having 2 levels of magnetization corresponding to $\mu^{-1} = 0.3$ and 0.1 as well as two angles between the rotation and magnetic field axis initially, namely 30° and 90° .

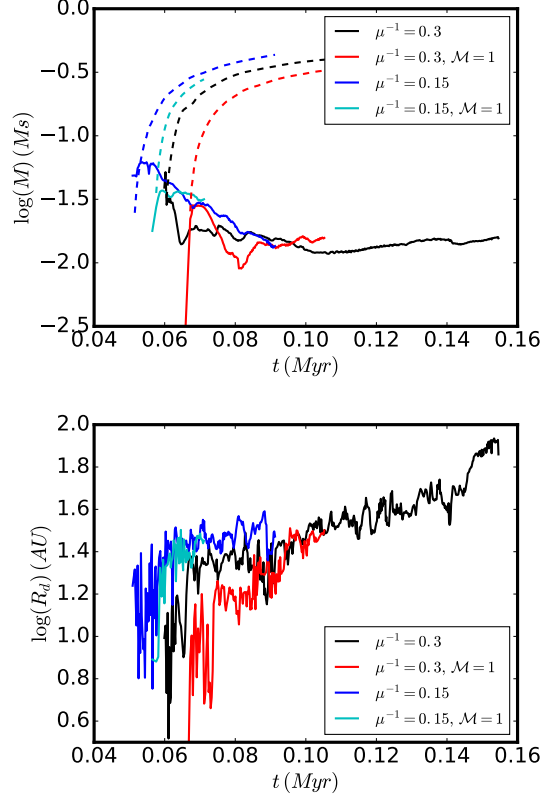


Fig. 11. Comparison between disc radius and mass for runs *R2*, *R4*, *R6* and *R8*, i.e. having 2 levels of magnetization corresponding to $\mu^{-1} = 0.3$ and 0.15 as well as two values of initial turbulent Mach number initially, namely 0 and 1 .

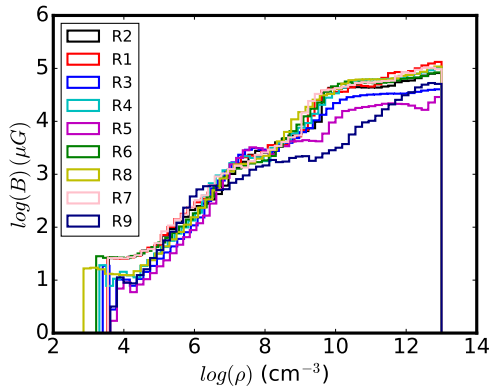


Fig. 12. Mean magnetic intensity as a function of density within the 9 runs. Apart for runs R3, R5 and R9 which all have $\mu^{-1} < 0.1$, i.e. a very low field initially, the distribution of the magnetic intensity is remarkably similar for all runs.

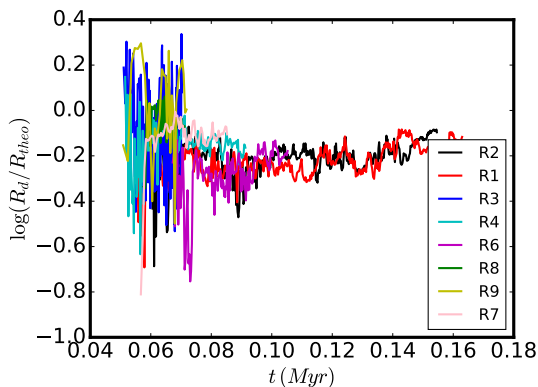


Fig. 13. Ratio of disc radius and theoretical prediction from Hennebelle et al. (2016) for runs R1-R9. As can be seen the analytical model leads to reasonable agreement with the simulations within a factor of about 2.

core in which non-ideal MHD operates, namely the ambipolar diffusion. The first series of runs explore the influence of the numerical parameters such as the numerical resolution and the sink particle accretion scheme. The goal of the second series of runs is to understand the impact of initial conditions on the disc properties. In particular, we vary the initial magnetic intensity, the rotation speed, the inclination of the field with respect to the rotation axis and the level of turbulence.

We found that while the mass of the central object is insensitive to the numerical scheme, the disc mass on the contrary depends significantly on the accretion scheme onto the sink particle. Essentially, at a given spatial resolution, the disc density increases with n_{acc} , the density above which the sink would accrete. This in particular implies that the disc mass increases with n_{acc} . For a given value of n_{acc} , the disc mass decreases if the resolution increases. This is because the sink particles act as an inner boundary and what matters is the density imposed at this boundary. We suggest that in reality, it is the small scale accretion, perhaps the star-disc interaction that determines, together with the disc transport properties, the disc density profile and therefore its mass distribution.

Exploring a large sets of initial conditions, we found that the most critical parameter is the magnetic intensity particularly when it becomes small, i.e. for $\mu^{-1} < 0.1$, for which the disc radius increases with μ . For $\mu^{-1} < 0.07$, we found that the disc

fragments, leading to a binary. For magnetisation larger than $\mu^{-1} > 0.15$ the disc properties do not change strongly with it. By changing the rotation speed from a $\beta_{\text{rot}} = 0.01$ to $\beta_{\text{rot}} = 0.04$, we found that at least in this range of parameter, it does not modify significantly the size of the disc for instance. The reason of this somewhat counter-intuitive result is that magnetic braking really controls the process of disc formation and more rotation also leads to larger toroidal field and more braking. The misalignment between rotation axis and magnetic field direction is found to play a minor role when the field is substantial ($\mu^{-1} = 0.3$) but has a major impact when the field is weak ($\mu^{-1} = 0.1$) in which case a large disc of about 100 AU in radius forms. Finally, the two runs that include turbulence present discs which are nearly identical to the discs formed in the absence of turbulence.

We conclude that the disc physical characteristics, and in particular its mass, are to a large extent determined by the local physical processes that is to say the collapse, the magnetic braking, the field diffusion, as well as an inner boundary condition possibly determined by the star-disc interaction. Only when the magnetic field is relatively weak, i.e. $\mu^{-1} < 0.15$, we do find that the resulting discs present significantly different properties.

The standard disc that forms in our simulations has a mass of about $10^{-2} M_{\odot}$ (which we stress depends on the accretion condition onto the central sink), a radius of 20-30 AU and is weakly magnetized in the inner part ($\beta_{\text{mag}} > 100$) and strongly magnetized in the outer part ($\beta_{\text{mag}} < 0.1$). At later time, as the envelope disappears, the inner part of the disc remains barely changed by the external part as the disc develops. It is characterized by a weaker β_{mag} and a stiff density profile (we estimate it to be broadly $\propto r^{-4}$).

Acknowledgements. We thank the anonymous referee for a detailed and helpful report which has improved the paper. This work was granted access to HPC resources of CINES and CCRT under the allocation x2014047023 made by GENCI (Grand Equipement National de Calcul Intensif). This research has received funding from the European Research Council under the European Community's Seventh Framework Programme (FP7/2007-2013 Grant Agreement no. 306483). Y.-N. Lee acknowledges the financial support of the UnivEarthS Labex program at Sorbonne Paris Cité (ANR-10-LABX-0023 and ANR-11-IDEX-0005-02). We thank the programme national de physique stellaire, the programme national de planétologie and the programme national de physique et chimie du milieu interstellaire for their supports.

References

- Allen, A., Li, Z.-Y., & Shu, F. H. 2003, *ApJ*, 599, 363
 Banerjee, R. & Pudritz, R. E. 2006, *ApJ*, 641, 949
 Béthune, W., Lesur, G., & Ferreira, J. 2017, *A&A*, 600, A75
 Bleuler, A. & Teyssier, R. 2014, *MNRAS*, 445, 4015
 Bouvier, J., Alencar, S. H. P., Harries, T. J., Johns-Krull, C. M., & Romanova, M. M. 2007, in *Protostars and Planets V*, ed. B. Reipurth, D. Jewitt, & K. Keil, 479
 Ciardi, A. & Hennebelle, P. 2010, *MNRAS*, 409, L39
 Dapp, W. B. & Basu, S. 2010, *A&A*, 521, L56
 Dapp, W. B., Basu, S., & Kunz, M. W. 2012, *A&A*, 541, A35
 Dutrey, A., Semenov, D., Chapillon, E., et al. 2014, in *Protostars and Planets VI*, ed. H. Beuther, R. S. Klessen, C. P. Dullemond, & T. Henning, 317
 Frank, A., Ray, T. P., Cabrit, S., et al. 2014, in *Protostars and Planets VI*, ed. H. Beuther, R. S. Klessen, C. P. Dullemond, & T. Henning, 451
 Fromang, S., Hennebelle, P., & Teyssier, R. 2006, *A&A*, 457, 371
 Galli, D., Lizano, S., Shu, F. H., & Allen, A. 2006, *ApJ*, 647, 374
 Gray, W. J., McKee, C. F., & Klein, R. I. 2018, *MNRAS*, 473, 2124
 Greaves, J. S. & Rice, W. K. M. 2010, *MNRAS*, 407, 1981
 Hennebelle, P. & Ciardi, A. 2009, *A&A*, 506, L29
 Hennebelle, P., Commerçon, B., Chabrier, G., & Marchand, P. 2016, *ApJ*, 830, L8
 Hennebelle, P. & Fromang, S. 2008, *A&A*, 477, 9
 Hennebelle, P. & Inutsuka, S.-i. 2019, *Frontiers in Astronomy and Space Sciences*, 6, 5
 Hennebelle, P. & Teyssier, R. 2008, *A&A*, 477, 25

- Hirano, S. & Machida, M. N. 2019, *MNRAS*, 485, 4667
- Inutsuka, S.-i. 2012, *Progress of Theoretical and Experimental Physics*, 2012, 01A307
- Joos, M., Hennebelle, P., & Ciardi, A. 2012, *A&A*, 543, A128
- Joos, M., Hennebelle, P., Ciardi, A., & Fromang, S. 2013, *A&A*, 554, A17
- Jørgensen, J. K., van Dishoeck, E. F., Visser, R., et al. 2009, *A&A*, 507, 861
- Krasnopolsky, R., Li, Z.-Y., Shang, H., & Zhao, B. 2012, *ApJ*, 757, 77
- Li, Z. Y., Banerjee, R., Pudritz, R. E., et al. 2014, in *Protostars and Planets VI*, ed. H. Beuther, R. S. Klessen, C. P. Dullemond, & T. Henning, 173
- Li, Z.-Y., Krasnopolsky, R., & Shang, H. 2013, *ApJ*, 774, 82
- Machida, M. N., Inutsuka, S.-i., & Matsumoto, T. 2006, *ApJ*, 647, L151
- Machida, M. N., Inutsuka, S.-i., & Matsumoto, T. 2014, *MNRAS*, 438, 2278
- Machida, M. N., Matsumoto, T., & Inutsuka, S.-i. 2016, *MNRAS*, 463, 4246
- Manara, C. F., Morbidelli, A., & Guillot, T. 2018, *A&A*, 618, L3
- Marchand, P., Commerçon, B., & Chabrier, G. 2018, *A&A*, 619, A37
- Marchand, P., Masson, J., Chabrier, G., et al. 2016, *A&A*, 592, A18
- Masson, J., Chabrier, G., Hennebelle, P., Vaytet, N., & Commerçon, B. 2016, *A&A*, 587, A32
- Masson, J., Teyssier, R., Mulet-Marquis, C., Hennebelle, P., & Chabrier, G. 2012, *ApJS*, 201, 24
- Masunaga, H. & Inutsuka, S.-i. 2000, *ApJ*, 531, 350
- Masunaga, H., Miyama, S. M., & Inutsuka, S.-i. 1998, *ApJ*, 495, 346
- Maurry, A. J., André, P., Hennebelle, P., et al. 2010, *A&A*, 512, A40
- Maurry, A. J., André, P., Testi, L., et al. 2019, *A&A*, 621, A76
- Mouschovias, T. C. & Spitzer, L., J. 1976, *ApJ*, 210, 326
- Murillo, N. M., Lai, S.-P., Bruderer, S., Harsono, D., & van Dishoeck, E. F. 2013, *A&A*, 560, A103
- Najita, J. R. & Kenyon, S. J. 2014, *MNRAS*, 445, 3315
- Ohashi, N., Saigo, K., Aso, Y., et al. 2014, *ApJ*, 796, 131
- Padovani, M., Hennebelle, P., & Galli, D. 2013, *A&A*, 560, A114
- Price, D. J. & Bate, M. R. 2007, *MNRAS*, 377, 77
- Pringle, J. E. 1981, *ARA&A*, 19, 137
- Santos-Lima, R., de Gouveia Dal Pino, E. M., & Lazarian, A. 2012, *ApJ*, 747, 21
- Seifried, D., Banerjee, R., Pudritz, R. E., & Klessen, R. S. 2013, *MNRAS*, 432, 3320
- Shu, F. H. 1977, *ApJ*, 214, 488
- Suriano, S. S., Li, Z.-Y., Krasnopolsky, R., & Shang, H. 2018, *MNRAS*, 477, 1239
- Testi, L., Birnstiel, T., Ricci, L., et al. 2014, in *Protostars and Planets VI*, ed. H. Beuther, R. S. Klessen, C. P. Dullemond, & T. Henning, 339
- Teyssier, R. 2002, *A&A*, 385, 337
- Tobin, J. J., Looney, L. W., Li, Z.-Y., et al. 2016, *ApJ*, 818, 73
- Tomida, K., Machida, M. N., Hosokawa, T., Sakurai, Y., & Lin, C. H. 2017, *ApJ*, 835, L11
- Tomida, K., Tomisaka, K., Matsumoto, T., et al. 2013, *ApJ*, 763, 6
- Tomida, K., Tomisaka, K., Matsumoto, T., et al. 2010, *ApJ*, 714, L58
- Tsukamoto, Y., Okuzumi, S., Iwasaki, K., Machida, M. N., & Inutsuka, S. 2018, *ApJ*, 868, 22
- Tsukamoto, Y., Okuzumi, S., Iwasaki, K., Machida, M. N., & Inutsuka, S.-i. 2017, *PASJ*, 69, 95
- Vaytet, N., Commerçon, B., Masson, J., González, M., & Chabrier, G. 2018, *A&A*, 615, A5
- Vorobyov, E. I., Skliarevskii, A. M., Elbakyan, V. G., et al. 2019, *arXiv e-prints*, arXiv:1905.11335
- Wurster, J. & Bate, M. R. 2019, *MNRAS*, 486, 2587
- Wurster, J., Bate, M. R., & Price, D. J. 2018, *MNRAS*, 476, 2063
- Wurster, J., Bate, M. R., & Price, D. J. 2019, *MNRAS*, 489, 1719
- Wurster, J. & Li, Z.-Y. 2018, *Frontiers in Astronomy and Space Sciences*, 5, 39
- Wurster, J., Price, D. J., & Bate, M. R. 2016, *MNRAS*, 457, 1037
- Zhao, B., Caselli, P., Li, Z.-Y., & Krasnopolsky, R. 2018, *MNRAS*, 473, 4868
- Zhao, B., Caselli, P., Li, Z.-Y., et al. 2016, *MNRAS*, 460, 2050

Appendix A: Disc profiles for runs *R2hsink* and *R3*

In this section we give more details, on two of the runs namely Run2hsink and *R3* that we recall differ from our reference run *R2* by a higher value of n_{thres} (i.e. the value at which the sink accretes) and a weaker magnetisation. The two discs are larger than the disc of *R2* and also more massive (5 and 8).

Figures A.1 and A.2 display the column density, the density in the equatorial plan, the β_{mag} as a function of radius for several timesteps. It also shows several velocities at a given snapshot. These plots can be compared with Fig. 3.

For run *R2hsink*, the most important difference comes from the central density that is 3-4 times higher, which is a direct consequence of the higher value of n_{thres} . The value of β_{mag} is also slightly higher because of higher density.

For run *R3*, the mean density profile is not very different from *R2* (the spiral structure is not seen on the 1D profile). The value of β_{mag} is about 2-4 times lower.

Apart from these differences, the other profiles tend to be remarkably similar.

Appendix B: Outflows

As it is the case in most MHD collapse calculations (e.g. Banerjee & Pudritz 2006; Machida et al. 2006; Ciardi & Hennebelle 2010; Tomida et al. 2010; Hirano & Machida 2019), prominent outflows due to the magneto-centrifugal mechanism (Frank et al. 2014) also develop in the present simulations and for the sake of completeness we present them here.

Appendix B.1: Outflow qualitative description

Figure B.1 portrays density slices on which the velocity field is overplotted at 3 different snapshots. From the top and middle panels, we see that a magnetized cavity with expanding motion starts developing early. Indeed the corresponding time is very close to the moment when the sink particle is being introduced in run *R2*. Interestingly the gas close to the sink and disc is infalling and it is only at a distance of a few tens of AU that it expands. The cavity is broadly aligned with the direction of the mean magnetic field. Bottom panel shows that the outflow persists at later time and becomes relatively faster. The cavities are asymmetrical and do not occupy the whole disc surface as accretion along the disc axis is still occurring.

Figure B.2 is identical to Fig. B.1 but shows run *R3* (which has $\mu^{-1} = 0.1$). Top panel shows again that the outflow starts early and is concomitant to the sink creation. Again the velocity close to the disc and sink reveals that the gas is infalling. Middle panel shows that the cavities develop in a rather symmetric way and occupy all the surface within and above the disc. Bottom panel shows a larger scale view about 10 kyr later. The outflow stays symmetrical and well collimated.

Appendix B.2: Outflow velocity and mass

To quantify further the outflows in our simulations, we have selected all computational cells which have a radial velocity that is positive (therefore expanding) and larger than 1 km s^{-1} . Figure B.3 displays the total mass within the flow as well as its maximum velocity for all the runs listed in Table 2 except for run *R9* which do not present outflow. The total mass remains below 1% of the sink mass, except initially when the sink has a low mass. It should be stressed however that after a few kyr, the outflows reach the boundary of the computational domain and therefore

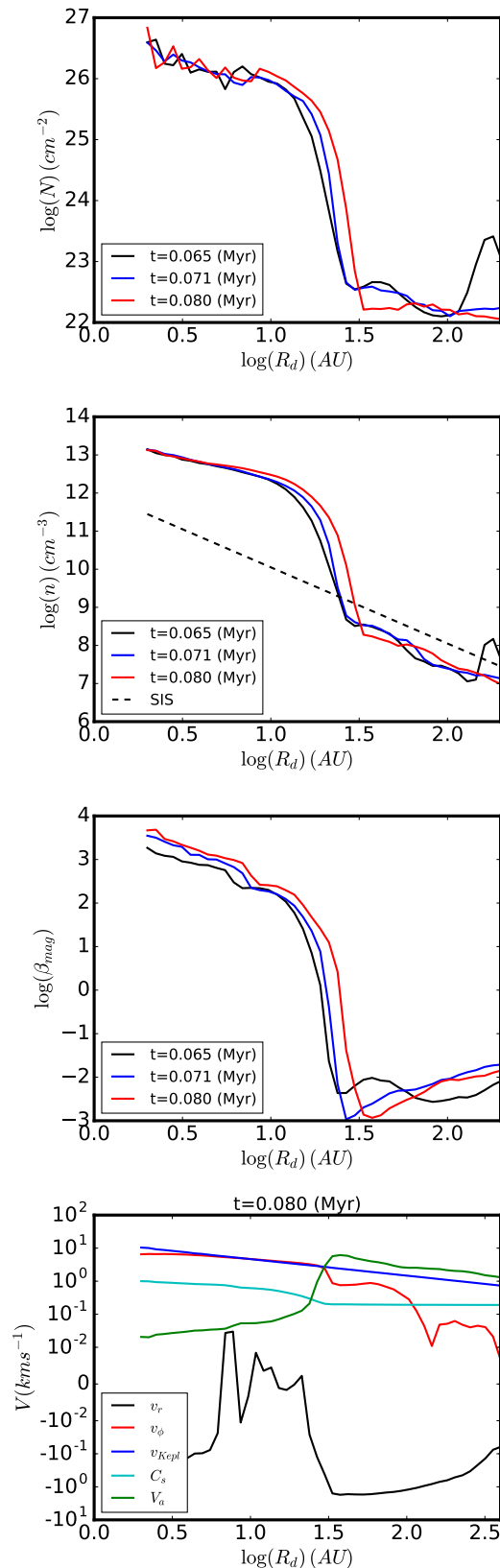


Fig. A.1. Radial structure of the disc of run *R2hsink* (i.e. $n_{\text{thres}} = 1.2 \cdot 10^{14} \text{ cm}^{-3}$). Top row: mean column density of the disc as a function of radius. Second panel: mean density of the disc vs radius. Third panel: $\beta_{\text{mag}} = P_{\text{therm}}/P_{\text{mag}}$ as a function of radius. Fourth panel: various velocities vs radius within the disc equatorial plane.

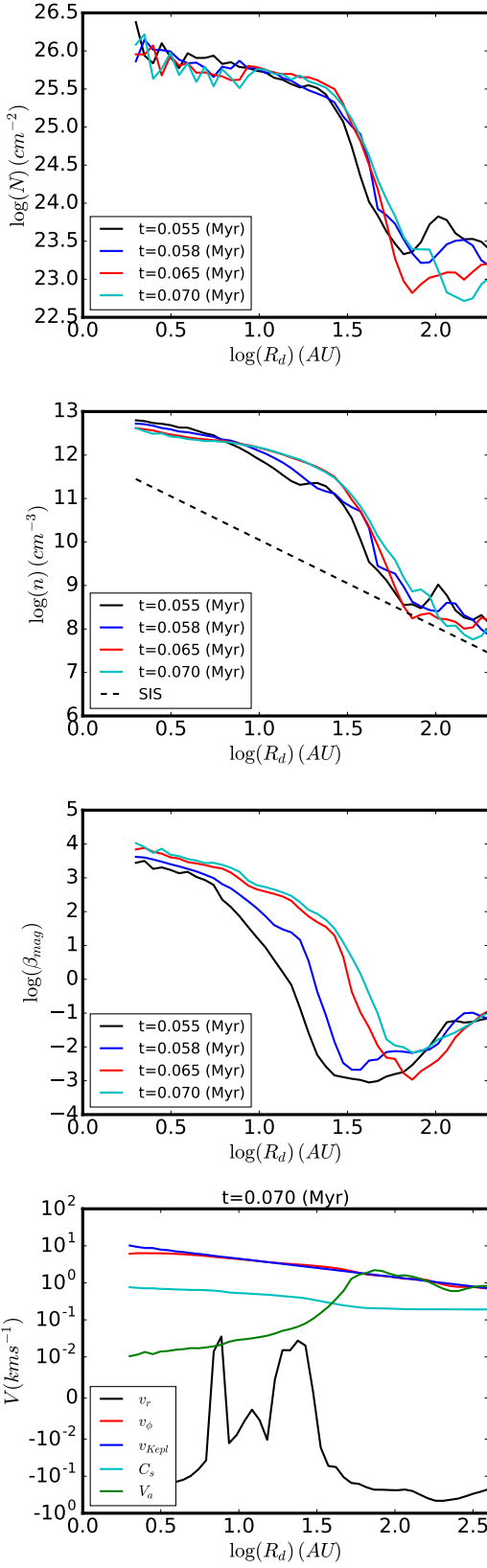


Fig. A.2. Radial structure of the disc of run R3 (i.e. $\mu^{-1} = 0.1$). Top row: mean column density of the disc as a function of radius. Second panel: mean density of the disc vs radius. Third panel: $\beta_{\text{mag}} = P_{\text{therm}}/P_{\text{mag}}$ as a function of radius. Fourth panel: various velocities vs radius within the disc equatorial plane.

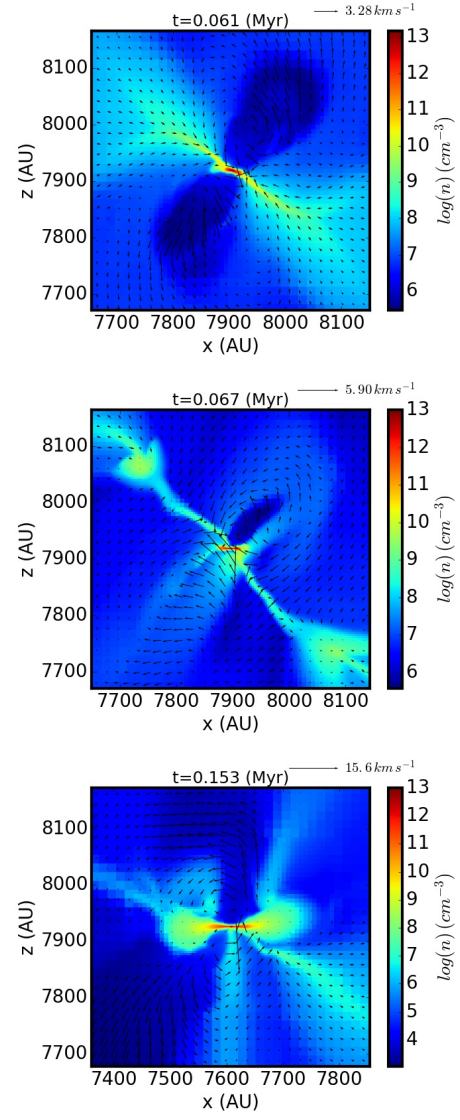


Fig. B.1. Density and velocity field at three snapshots for run R2.

the mass is not properly counted. The velocity threshold used to define the flow is obviously critical. Choosing smaller values, obviously leads to higher estimate but there is then a confusion with the expanding envelope which surrounds the core since the medium outside the core has initially a low pressure. The largest velocity within the flow tends to be similar in all runs and goes from about 5 km s^{-1} at early times to 15 km s^{-1} at later ones.

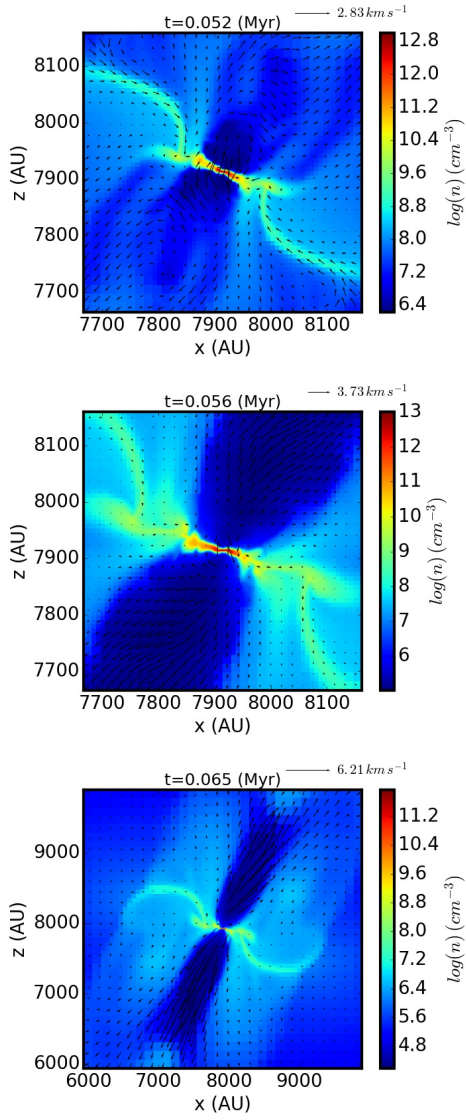


Fig. B.2. Density and velocity field at three snapshots for run R3.

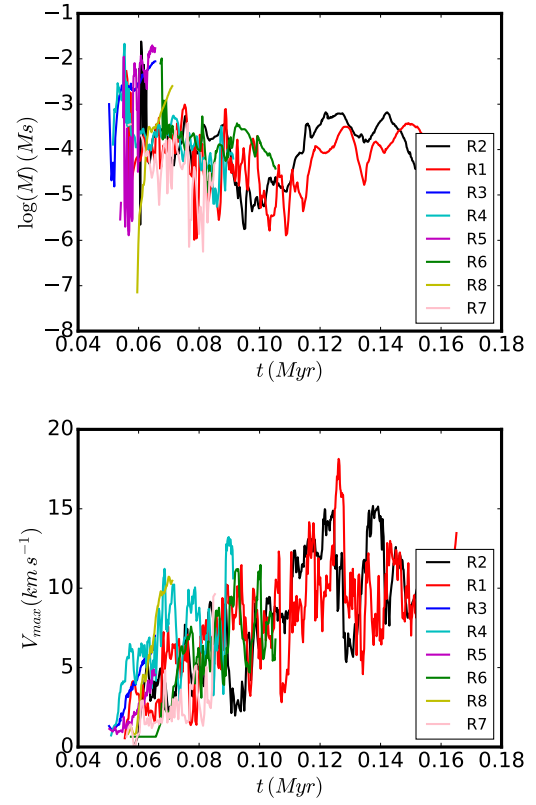


Fig. B.3. Top panel and bottom panel show respectively the mass within and the largest velocity of, the outflow defined as gas having a positive radial velocity larger than 1 km s^{-1} for all runs (except run R9 which presents no outflow).